

Search for supersymmetry in diphoton final states with the CMS detector

Matthew Lawrence Joyce

August 12, 2021

CONTENTS

1.	<i>The Standard Model of Particle Physics</i>	8
1.1	The Standard Model	8
1.2	Electroweak Symmetry Breaking	9
1.3	Problems with the SM	14
2.	<i>Supersymmetry</i>	16
3.	<i>The Large Hadron Collider</i>	17
3.1	Introduction	17
3.2	Injection Complex	17
3.3	Tunnel and Magnets	18
3.4	Luminosity	18
4.	<i>Compact Muon Solenoid</i>	24
4.1	Introduction	24
4.2	Coordinate System	25
4.3	Tracker	26
4.3.1	Pixel Detector	27
4.3.2	Strip Detector	28
4.4	Electromagnetic Calorimeter	29
4.4.1	Crystals	29
4.4.2	Barrel and Endcaps	30
4.4.3	Preshower layer	31
4.4.4	Performance	31
4.5	Hadronic Calorimeter	32
4.6	Superconducting Solenoid	33
4.7	Muon System	34
5.	<i>MIP Timing Detector (MTD)</i>	37
5.1	Introduction	37
5.2	Barrel Timing Layer	39
5.2.1	LYSO:Ce crystals	43

5.2.2	SiPMs	46
5.2.3	Glue qualification	47
5.2.4	Performance at test beam	49
6.	<i>CMS Trigger System</i>	53
6.1	L1 trigger	53
6.1.1	Calorimeter trigger	53
6.1.2	Muon trigger	55
6.1.3	Global Trigger	55
6.2	High Level Trigger	55
6.3	Trigger efficiency	56
7.	<i>CMS Particle and Event Reconstruction</i>	57
7.1	Tracks	57
7.2	Calorimeter clusters	58
7.3	Object identification	58
7.3.1	Muons	58
7.3.2	Electrons	59
7.3.3	Photons	60
7.3.4	Jets	61
7.4	Missing transverse momentum	61
8.	<i>Data Analysis</i>	62
8.1	Overview	62
8.2	Data	62
8.3	Monte Carlo samples	63
8.4	Object definitions	63
8.4.1	Photons	64
8.4.2	Electrons	65
8.4.3	Muons	65
8.4.4	Jets	65
8.5	Backgrounds	65
8.5.1	Instrumental background	66
8.5.2	Electroweak background	69
8.5.3	Irreducible background	69

LIST OF FIGURES

1.1	Illustration of the Higgs potential for $\mu^2 < 0$	13
1.2	Summary of content of the SM.	15
3.1	LHC interaction points	20
3.2	Layout of LHC accelerator complex [17].	21
3.3	Proton bunch capture onto RF bucket [7].	22
3.4	Cross section of LHC dipole [10]	22
3.5	Integrated luminosity delivered by the LHC to the CMS experiment each year from 2010-2018.	23
4.1	Schematic of CMS detector [25]	25
4.2	Transverse slice of the CMS detector[8].	26
4.3	Cross section (side) of CMS tracker prior to the Phase 1 upgrade during the year-end technical stop of 2016/2017. Each line represents a detector module while double lines indicate back-to-back strip modules. Surrounding the pixel tracker (PIXEL) is the strip detector, which is divided into the Tracker Inner Barrel (TIB), Tracker Outer Barrel (TOB), Tracker Inner Disks (TID), and Tracker Endcaps (TEC). Reprinted from Reference [13].	27
4.4	Cross section (side) of pixel detector. The lower half , labeled "Current", shows the design prior to 2017 while the upper half, labeled "Upgrade", shows the design after the upgrade. Reprinted from Resource [12]	28
4.5	PbWO ₄ crystals. Left: EB crystal with APD. Right: EE crystal with VPT. Reprinted from [14]	30
4.6	Schematic of ECAL. Reprint from [14]	32
4.7	Longitudinal view of HCAL [2]	34
4.8	Longitudinal slice of CMS detector while operating at 3.8-T central magnetic field. The right-hand side of the figure shows a mapping of the magnetic field lines while the left-hand side shows a mapping of the field strength. Reprint from [11] . . .	35

4.9	Cross-section of one quadrant of the CMS detector. The DTs are labeled as "MB" (Muon Barrel) and the CSCs are labelled as "ME" (Muon Endcap). The RPCs are "RB" for those in the barrel and "RE" for those in the endcap. Reprint from [27].	36
5.1	Timeline for LHC	37
5.2	Vertices from a simulated 200 pileup event with MTD timing resolution of ~ 30 ps. The red dots represent the simulated vertices while the yellow lines indicate vertices reconstructed without the use of timing information. The black crosses and blue open circles represent tracks and vertices reconstructed using time information from the MTD. Reprint from	38
5.3	Schematic view of MTD	39
5.4	LYSO:Ce crystal slant thickness in the BTL.	41
5.5	Overview of the BTL	42
5.6	Readout unit for the BTL.	43
5.7	Evolution of time resolution for the BTL.	44
5.8	Transmission curve for LYSO:Ce before and after being irradiated to a fluence of $2 \times 10^{13} \text{ cm}^{-2}$ with 24 GeV protons.	45
5.9	Time resolution measurements of LYSO:Ce before and after irradiation.	46
5.10	Energy spectrum for Cs^{137}	48
5.11	Left: This is a teflon mold used to produce glue samples. Right: The glue samples after being removed from the mold. These samples were then placed in the irradiator for radiation exposure.	49
5.12	Preliminary radiation tolerance studies of the top five glue candidates show that only NOA-61 and RTV-3145 are viable. Epotek, Polytec, and BC-600 all show substantial optical degradation after just a fraction of 50 kGy target.	50
5.13	Figure 5.13a shows an example a glue sample ready for transmission measurements. Figure 5.13b shows how the measurement is taken with the sample placed inside the photospectrometer.	51
5.14	Transmission curves for both NOA-61 (Figure 5.14a and RTV-3145 (Figure 5.14b). Figure 5.14c shows the transmission at 420 nm, the peak of the LYSO:Ce emission spectrum, with increasing ionizing doses. While NOA-61 starts with a higher transmission, RTV-3145 is more radiation tolerant and has a higher transmission after the full ionizing dose.	52

6.1	L1 trigger system. Reprint from [3]	54
7.1	The Bremsstrahlung photons continue along a straight trajectory while the electron path is bent by the magnetic field. This results in energy deposited in the calorimeter for such electrons to be spread out along the ϕ -direction.	60
8.1	Two examples of GGM supersymmetry breaking processes resulting in final states containing two photons and missing transverse momentum. The T5gg model (left) shows gluinos produced from $p - p$ collisions which subsequently result in two neutralinos, each decaying to a photon and a gravitino. The T6gg model (right) shows squarks produced from $p - p$ collisions following a similar decay chain.	62
8.2	Mismeasurement of Jet3 results in an imbalance in the events transverse momentum.	66
8.3	The 95% confidence level upper limits on the pair production cross sections for gluinos (8.3a) and squarks (8.3b) as a function of gluino/squark and neutralino masses as reported in [26]. The shaded vertical bands show the mass bands used in the BDT training.	71
8.4	BDT input variables	72
8.5	BDT training and testing results	73
8.6	BDT cut values on T5GG models resulting in 90% signal acceptance.	74
8.7	BDT cut values on T6GG models resulting in 90% signal acceptance.	75
8.8	BDT response to Rebalance and Smear events in GJets MC .	76

LIST OF TABLES

1.1	Boson fields in the SM	9
1.2	Fermions in the SM. The first two numbers listed in the third column give the supermultiplet representation under $SU(3)_C$ and $SU(2)_L$ respectively. A 1 means that it is not charged under that group and therefore will not couple to the associated force. A 3 as the first number means that it has color charge and couples to the strong force. A 2 for the second number means that it has weak isospin and couples to the weak force. The third number gives the value of the weak isospin. Adjoint representation is specified by the presence of a bar over the number.	10
4.1	Summary of signals expected for each particle type in each sub-detector.	24
5.1	Predicted radiation doses and fluences at different location of the BTL after an integrated luminosity of 3000 fb^{-1} . The two far right columns include a safety margin of 1.5.	40
5.2	Summary of crystal and slant thicknesses in different η regions.	41
6.1	Primary HLT	56
8.1	Data Samples	63
8.2	Summary of loose ID photons cuts	64
8.3	List of MC samples used for training and testing BDT	68
8.4	Summary of $Z\gamma\gamma \rightarrow \nu\nu\gamma\gamma$ model validation	70

¹ 1. THE STANDARD MODEL OF PARTICLE PHYSICS

² 1.1 *The Standard Model*

The Standard Model (SM) of particle physics is a Lorentz-invariant quantum field theory (QFT) that describes the dynamics of elementary particles. Three critical developments leading to the formation of the SM, as described by Steven Weinberg[28], were the quark model proposed by Gell-Mann[19] and Zweig[31] in 1964, the idea of gauge symmetry by Yang and Mills[30] in 1954, and the notion of spontaneous symmetry breaking proposed by Goldstone[20] in 1961. This ultimately led to the SM in its current form as a non-Abelian gauge theory with the symmetry group

$$G_{SM} = SU(3)_C \otimes SU(2)_L \otimes U(1)_Y \quad (1.1)$$

³ where $SU(3)_C$ is responsible for strong interactions and $SU(2)_L \otimes U(1)_Y$ is
⁴ responsible for unified electromagnetic and weak interactions, also known as
⁵ electroweak interactions.

⁶ Associated with each of these symmetry groups is a set of massless spin-1
⁷ vector fields called gauge bosons. These are listed in Table 1.1 along with the
⁸ associated charge or generator for that group. There are eight such gauge
⁹ bosons in $SU(3)_C$ called gluons $G_\mu^{1,\dots,8}$. There are three gauge bosons $W_\mu^{1,2,3}$
¹⁰ in $SU(2)_L$ and one gauge boson B_μ in $U(1)_Y$. The gauge bosons mediate
¹¹ the interactions between spin-1/2 fields ψ called fermions. At this point
¹² it's worth noting that the W and B gauge fields are not observable bosons,
¹³ but are mixed by electroweak symmetry breaking to produce observable
¹⁴ bosons. The details of this will be covered in Section 1.2.

¹⁵ There are twelve fermion fields which can be split into six lepton fields
¹⁶ and six quark fields. Both quarks and leptons are comprised of three genera-
¹⁷ tions. For quarks there are three "up-type" quarks (up u , charm c , and top
¹⁸ t) and three "down-type" quarks (down d , strange s , and bottom b). The
¹⁹ lepton fields are electron e , muon μ , tau τ , and three neutrino fields ν_e , ν_μ ,
²⁰ and ν_τ . The fermion fields and their representations under G_{SM} are listed
²¹ in Table 1.2. Each fermion field can be expressed in terms of left and right

²² chirality fields, which are represented by a doublets ψ_L in the left-handed
²³ case and singlets ψ_R in the right-handed case with

$$\psi = \psi_R + \psi_L \quad (1.2)$$

$$\psi_R = \frac{1}{2}(1 + \gamma^5)\psi \quad (1.3)$$

$$\psi_L = \frac{1}{2}(1 - \gamma^5)\psi \quad (1.4)$$

²⁴ The SM also contains a complex scalar doublet field ϕ called the Higgs
²⁵ field in honor of Peter Higgs, who was among one of the physicists who
²⁶ proposed its existence in 1964 [22].

Tab. 1.1: Boson fields in the SM

Symbol	Associated Charge	Symmetry group
B_μ	weak hypercharge Y	$U(1)_Y$
$G_\mu^{1,\dots,8}$	color $C = (r, g, b)$	$SU(3)_C$
$W_\mu^{1,2,3}$	weak isospin T_3	$SU(2)_L$

The strong interaction is described by the theory of quantum chromodynamics (QCD). The Lagrangian for the QCD interaction can be written as

$$\mathcal{L}_{QCD} = \bar{\psi}(i\gamma^\mu D_\mu - m)\psi - \frac{1}{2}TrG_{\mu\nu}G^{\mu\nu} \quad (1.5)$$

²⁷ where

$$G_{\mu\nu} = \partial_\mu G_\nu - \partial_\nu G_\mu - ig_s[G_\mu, G_\nu] \quad (1.6)$$

$$D_\mu = \partial_\mu - ig_s G_\mu \quad (1.7)$$

²⁸ g_s is related to the strong coupling constant, and m is the fermion mass,
²⁹ which in this case must be a quark since they are the only fermions with
³⁰ color charge.

³¹ 1.2 Electroweak Symmetry Breaking

A crucial feature of the SM is electroweak symmetry breaking. The electroweak interaction, first proposed by Glashow, Weinberg, and Salam in the 60's, is the unified description of electromagnetic and weak interactions under the $SU(2)_L \otimes U(1)_Y$ symmetry. The electromagnetic interaction is described by quantum electrodynamics (QED), which is an Abelian gauge

Tab. 1.2: Fermions in the SM. The first two numbers listed in the third column give the supermultiplet representation under $SU(3)_C$ and $SU(2)_L$ respectively. A **1** means that it is not charged under that group and therefore will not couple to the associated force. A **3** as the first number means that it has color charge and couples to the strong force. A **2** for the second number means that it has weak isospin and couples to the weak force. The third number gives the value of the weak isospin. Adjoint representation is specified by the presence of a bar over the number.

Name	Notation	Representation under $SU(3)_C \otimes SU(2)_L \otimes U(1)_Y$
Left-handed quark doublet	$\begin{pmatrix} u_L \\ d_L \end{pmatrix}, \begin{pmatrix} c_L \\ s_L \end{pmatrix}, \begin{pmatrix} t_L \\ b_L \end{pmatrix}$	(3, 2, $\frac{1}{6}$)
Right-handed up-type quark singlet	$u_R^\dagger, c_R^\dagger, b_R^\dagger$	($\bar{3}$, 1, $-\frac{2}{3}$)
Right-handed down-type quark singlet	$d_R^\dagger, s_R^\dagger, t_R^\dagger$	($\bar{3}$, 1, $\frac{1}{3}$)
Left-handed lepton doublet	$\begin{pmatrix} \nu_{eL} \\ e_L \end{pmatrix}, \begin{pmatrix} \nu_{\mu L} \\ \mu_L \end{pmatrix}, \begin{pmatrix} \nu_{\tau L} \\ \tau_L \end{pmatrix}$	(1, 2, $-\frac{1}{2}$)
Right-handed charged lepton singlet	$e_R^\dagger, \mu_R^\dagger, \tau_R^\dagger$	($\bar{1}$, 1, 1)

theory under the $U(1)_{EM}$ symmetry group. The gauge boson in QED is the photon and couples to electric charge Q . The QED Lagrangian is given by

$$\mathcal{L}_{QED} = \bar{\psi}(i\gamma^\mu D_\mu - m)\psi - \frac{1}{4}F_{\mu\nu}F^{\mu\nu} \quad (1.8)$$

³² where

$$F_{\mu\nu} = \partial_\mu A_\nu - \partial_\nu A_\mu \quad (1.9)$$

$$D_\mu = \partial_\mu + ieQA_\mu \quad (1.10)$$

³³ and A_μ is the electromagnetic or photon field.

The Lagrangian for the unbroken $SU(2)_L \otimes U(1)_Y$ symmetry is given by

$$\mathcal{L}_{EW} = \bar{\psi}i\gamma^\mu D_\mu\psi - Tr\frac{1}{8}W_{\mu\nu}W^{\mu\nu} - \frac{1}{4}B_{\mu\nu}B^{\mu\nu} \quad (1.11)$$

³⁴ where

$$W_{\mu\nu} = \partial_\mu W_\nu - \partial_\nu W_\mu - ig_w[W_\mu, W_\nu] \quad (1.12)$$

$$B_{\mu\nu} = \partial_\mu B_\nu - \partial_\nu B_\mu \quad (1.13)$$

with a separate fermion term for each field ψ_R and ψ_L . The covariant derivative D_μ is given by

$$D_\mu = \partial_\mu + ig_wT_iW_\mu^i + ig_Y\frac{Y}{2}B_\mu \quad (1.14)$$

³⁵ with W_μ^i and T_i written in terms of raising and lowering operators

$$W_\mu^\pm = \frac{1}{\sqrt{2}}(W_\mu^1 \mp W_\mu^2) \quad (1.15)$$

$$T^\pm = \frac{1}{\sqrt{2}}(T_1 \pm T_2) \quad (1.16)$$

$$W_\mu^0 = W_\mu^3 \quad (1.17)$$

$$T^0 = T_3 \quad (1.18)$$

The neutral portion of the covariant derivative $ig_wT_3W_\mu^3 + ig_Y\frac{Y}{2}B_\mu$ must contain the electromagnetic term $ieAQ$ for the electromagnetic interaction to be unified with the weak interaction, so the W_μ^3 and B_μ fields need to linear combinations of the photon field A_μ and another field Z_μ . This relationship can be written in terms of the electroweak mixing angle θ_w , also known as the Weinberg angle, as

$$\begin{pmatrix} A_\mu \\ Z_\mu \end{pmatrix} = \begin{pmatrix} \cos\theta_W & \sin\theta_W \\ -\sin\theta_W & \cos\theta_W \end{pmatrix} \begin{pmatrix} B_\mu \\ W_\mu^3 \end{pmatrix} \quad (1.19)$$

The weak isospin T_3 and weak hypercharge Y can be related to the electric charge Q with the Gell-Mann-Nishijima formula

$$Y = 2(Q - T_3) \quad (1.20)$$

³⁶ and the coupling constants g_w , g_Y , and e are related to the mixing angle by

$$e = g_w \cos \theta_W = g_Y \sin \theta_W \quad (1.21)$$

$$\sin \theta_W = \frac{g_Y}{\sqrt{g_w^2 + g_Y^2}} \quad (1.22)$$

$$\cos \theta_W = \frac{g_w}{\sqrt{g_w^2 + g_Y^2}} \quad (1.23)$$

At this point the $W_\mu^{1,2,3}$ and B_μ fields have been mixed to produce the observable fields W_μ^+ , W_μ^- , A_μ , and Z_μ , but this is still inconsistent with experimental observations as these bosons and all of the fermions are still massless in this model. In order to generate the masses while maintaining the renormalizability of the gauge theory the symmetry needs to be spontaneously broken. This is done by the introduction of a complex scalar doublet field called the Higgs field which is expressed as

$$\phi = \begin{pmatrix} \phi^+ \\ \phi^0 \end{pmatrix} = \frac{1}{\sqrt{2}} \begin{pmatrix} \phi_1 + i\phi_2 \\ \phi_3 + i\phi_4 \end{pmatrix} \quad (1.24)$$

where the fields ϕ_i are real scalar fields. The Lagrangian for the Higgs field is

$$\mathcal{L}_{Higgs} = (D_\nu \phi)^\dagger (D^\nu \phi) - V(\phi^\dagger \phi) \quad (1.25)$$

with the potential $V(\phi^\dagger \phi)$ being given by

$$V(\phi^\dagger \phi) = \mu^2 \phi^\dagger \phi + |\lambda| (\phi^\dagger \phi)^2 \quad (1.26)$$

and the covariant derivative

$$D_\nu = \partial_\nu - \frac{i}{2} g_w W_\nu^i \sigma_i - \frac{i}{2} g_Y B_\nu \quad (1.27)$$

Since $\mu^2 < 0$, this potential has the shape of a sombrero as is shown in Figure 1.1. The scalar fields have some positive vacuum expectation value (VEV) satisfying

$$\phi^\dagger \phi = v = \sqrt{-\frac{\mu^2}{\lambda}} \quad (1.28)$$

at the minimum which allows us to write the ground state as

$$\phi_{ground} = \langle 0 | \phi | 0 \rangle = \frac{1}{\sqrt{2}} \begin{pmatrix} 0 \\ v \end{pmatrix} \quad (1.29)$$

Expanding the Higgs field about it's minimum as

$$\phi_{ground} \rightarrow \phi(x) = \frac{1}{\sqrt{2}} e^{i\sigma_\alpha \theta^\alpha(x)} \begin{pmatrix} 0 \\ v + h(x) \end{pmatrix}, \alpha = 1, 2, 3 \quad (1.30)$$

results in a massive field $h(x)$ and three massless scalar fields, or Goldstone bosons, $\theta_{1,2,3}$ which represent degrees of freedom. By then transforming into the unitary gauge we can remove the phase factor, thereby eliminating the explicit appearance of the three Goldstone bosons in the Lagrangian. In gauging away the Goldstone bosons, the three degrees of freedom reappear as longitudinal polarization states of the W^+ , W^- , and Z bosons. In other words, the W and Z bosons have become massive by "eating" the Goldstone bosons.

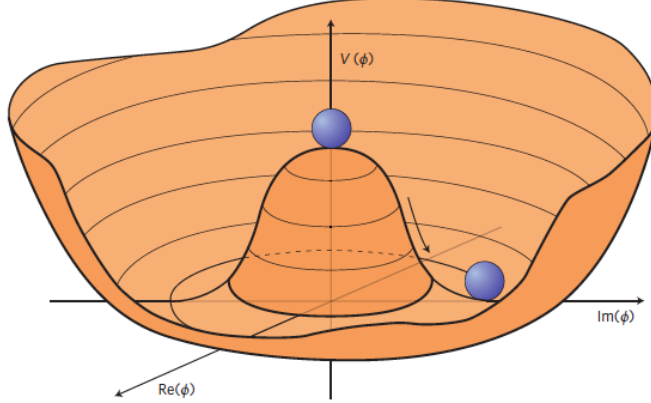


Fig. 1.1: The Higgs potential is shown as a function of the complex scalar field's real and imaginary parts. The balls illustrate that the stable vacuum state of nature is not located at $\phi = 0$ because the symmetry at that point is spontaneously broken. Instead the stable vacuum state of nature is located somewhere along the circle of minimum potential. Reprint from [5]

Writing the Lagrangian in Equation 1.25 in terms of the physical W and

Z fields and evaluating at the VEV gives

$$\begin{aligned}\mathcal{L}_{Higgs} = & \frac{1}{2}\partial_\nu h\partial^\nu h + \frac{1}{4}g_w^2 W_\nu^+ W^{-\nu}(v+h)^2 \\ & + \frac{1}{8\cos^2\theta_W}Z_\nu Z^\nu(v+h)^2 - V[\frac{1}{2}(v+h)^2]\end{aligned}\quad (1.31)$$

₄₅ The v^2 terms give the W and Z boson masses and the h^2 term gives the
₄₆ mass of the Higgs boson as

$$M_W = \frac{1}{2}g_w v \quad (1.32)$$

$$M_Z = \frac{1}{2}v \frac{g_w}{\cos\theta_W} = \frac{M_W}{\cos\theta_W} \quad (1.33)$$

$$M_H = \sqrt{2}|\mu| \quad (1.34)$$

₄₇ while the photon remains massless.

₄₈ At this point we can summarize the particle content of the SM and their
₄₉ allowed interactions in a way that is seen in Figure 1.2.

₅₀ *1.3 Problems with the SM*

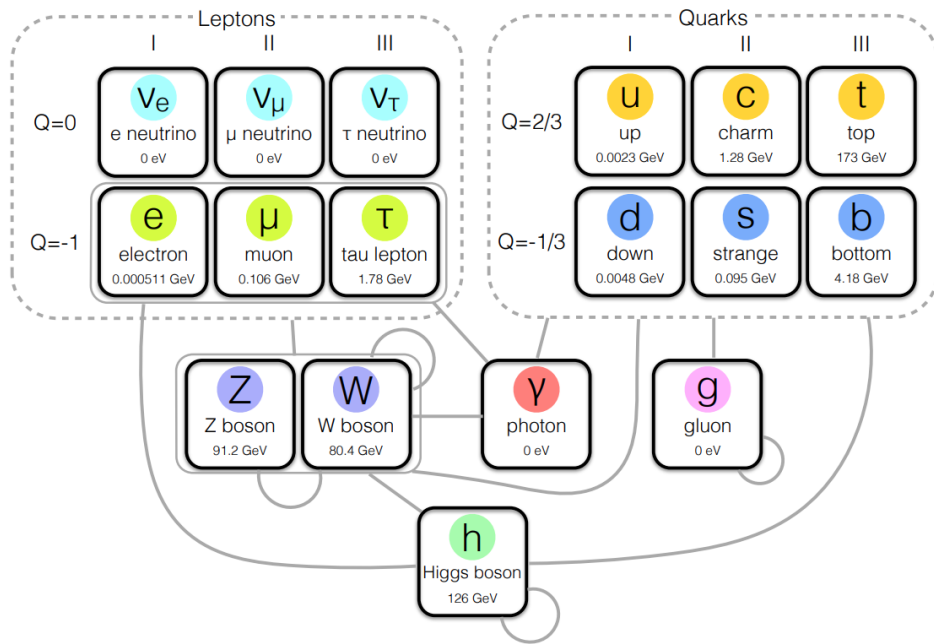


Fig. 1.2: Summary of particle content in the SM. Gray lines connecting groups of particles indicates allowed interactions. Self-coupling is indicated by a gray line connecting a particle to itself. The leptons and quarks are organized in columns corresponding to generation, which is specified at top, and rows corresponding to electric charge Q , which is listed to the left. Each particle's mass is listed beneath its name and symbol. It should be noted that neutrinos in the SM are still treated as massless leptons despite the fact that experimental evidence has established that at least two of the neutrinos are massive. Reprinted from [23]

2. SUPERSYMMETRY

52

3. THE LARGE HADRON COLLIDER

53

3.1 Introduction

54 The Large Hadron Collider (LHC) is a 26.7 kilometer-long, two-ring particle
 55 accelerator and collider located on the border of France and Switzerland at
 56 the European Organization for Nuclear Research (CERN). During normal
 57 operations the LHC maintains two counter-rotating beams of proton bunches
 58 that collide at four interaction points (IP) with up to $\sqrt{s} = 14$ TeV center
 59 of mass energy and a luminosity of $10^{34}\text{cm}^{-2}\text{s}^{-1}$. The ALICE (Point 2),
 60 ATLAS (Point 1), CMS (Point 5), and LHC-b experiments each have a
 61 detector at one of these interaction points as scene in Figure 3.1 . The CMS
 62 and ATLAS are general-purpose detectors while LHC-b specializes in beauty
 63 quark studies. ALICE is a heavy-ion experiment which uses $^{208}\text{Pb} - p$ or
 64 $^{208}\text{Pb} - ^{208}\text{Pb}$ collisions that can also be produced by the LHC.

65

3.2 Injection Complex

66 In order to bring the protons from rest up to their target collision energy
 67 a series of accelerators, as shown in Figure 3.2, are used. The acceleration
 68 sequence begins with the injection of hydrogen gas into a duoplasmatron.
 69 Here a bombardment of electrons ionize the hydrogen atoms while an electric
 70 field pushes them through the duoplasmatron cavity. The result is 100 keV
 71 protons being passed on to a quadrupole magnet which guides them into
 72 the aperture of a linear accelerator (LINAC2). The radio frequency (RF)
 73 cavities in LINAC2 accelerate the protons up to 50 MeV. At this point the
 74 protons are sent into one of four rings in the Proton Synchrotron Booster
 75 (PSB). The PSB repeatedly accelerates the protons around a circular path
 76 until they reach an energy of 1.4 GeV. The bunches of protons from each PSB
 77 ring are then sequentially injected into the single-ringed Proton Synchrotron
 78 (PS). Each bunch injected into the PS are captured by one of the "buckets"
 79 (Figure 3.3) provided by the PS RF system which also manipulates the
 80 bunches into the desired profile and proton density. These proton bunches
 81 are accelerated to 25 GeV and injected into the Super Proton Synchrotron

(SPS) where they are accelerated to 450 GeV. Finally the proton bunches are injected into the LHC ring where they are accelerated to 6.5 TeV and collided in 25 ns intervals to yield a center of mass energy of $\sqrt{s} = 13$ TeV.

3.3 Tunnel and Magnets

The LHC was designed to produce collisions with up to $\sqrt{s} = 14$ TeV. That requires confining and guiding 7 TeV protons around the circumference of the LHC ring. The ring is housed in a 4 meter-wide underground tunnel that ranges in depth between 45 and 170 meters below the surface. This tunnel was repurposed from the Large Electron-Positron (LEP) Collider which previously occupied the space. For this reason the tunnel is not completely circular but is instead made up of alternating curved and straight sections of 2500 m and 530 m in length respectively. The straight sections, labeled 1-8 in Figure 3.1, are used as either experimental facilities or sites for hardware necessary for LHC operations such as RF cavities for momentum cleaning, quadrupole magnets for beam focusing, and sextupole magnets for acceleration and betatron cleaning.

Steering a 7 TeV proton beam around the curved sections requires a magnetic field of 8.33 Tesla which is provided by 1223 superconducting dipole magnets cooled to 1.9 K. A cross section of the LHC dipole is shown in Figure 3.4. Supercooled liquid helium flows through the heat exchanger pipe to cool the iron yolk to a temperature of 1.9 K. Ultra high vacuum is maintained in the outer volume to provide a layer of thermal insulation between the inner volume and the outer steel casing. Inside the iron yolk is a twin bore assembly of niobium-titanium superconducting coils. Two parallel beam pipes are located within the focus of the superconducting coils. This is the ultra high vacuum region where the subatomic particles are confined as they travel around the LHC ring.

3.4 Luminosity

The number of events generated per second for specific process having cross-section σ_{event} is given by:

$$\frac{dN_{event}}{dt} = L\sigma_{event} \quad (3.1)$$

where L is the machine luminosity. The machine luminosity for a Gaussian beam distribution can be written in terms of the beam parameters as:

$$L = \frac{N_b^2 n_b f_{rev} \gamma_r}{4\pi \epsilon_n \beta_*} F \quad (3.2)$$

where N_b is particle density in each bunch, n_b is the number of bunches in each beam, f_{rev} is the frequency of revolution, and γ_r is the relativistic gamma factor. The variables ϵ_n and β_* are the normalized transverse beam emittance and the beta function at the IP respectively, while F is the geometric reduction factor depending due to the beams' crossing angle at the IP. [17]

The total number of events produced over a given amount of time would then be

$$N_{event} = \sigma_{event} \int L dt = \sigma_{event} L_{integrated}. \quad (3.3)$$

The integrated luminosity delivered each year to the CMS experiment is shown in 3.5. The analysis presented here uses data collected from the 2016, 2017, and 2018 campaigns which gives a combined integrated luminosity of 158.7 fb^{-1} .

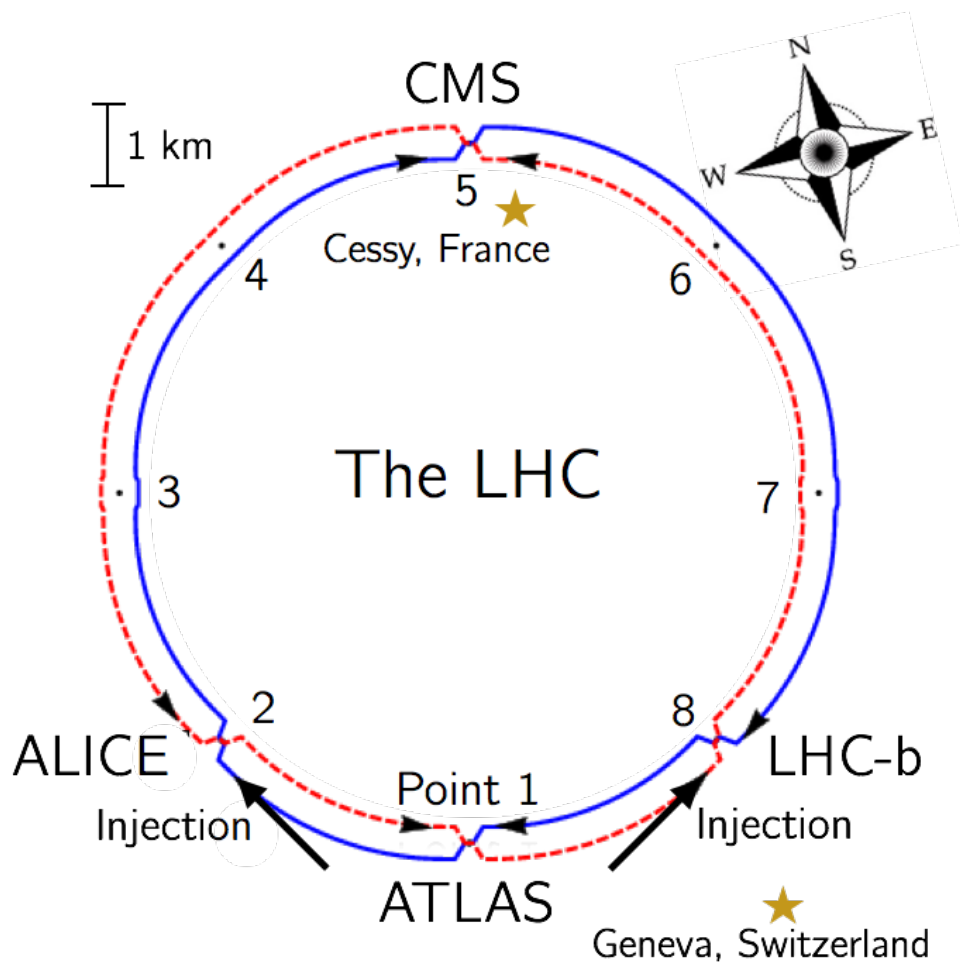


Fig. 3.1: Interaction points of the LHC

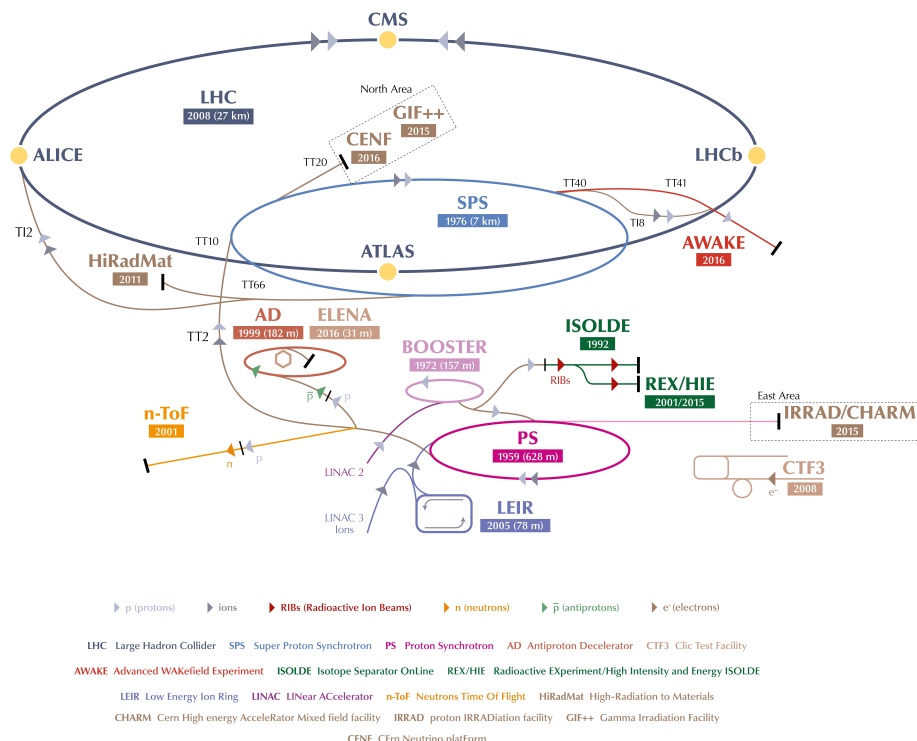


Fig. 3.2: Layout of LHC accelerator complex [17].

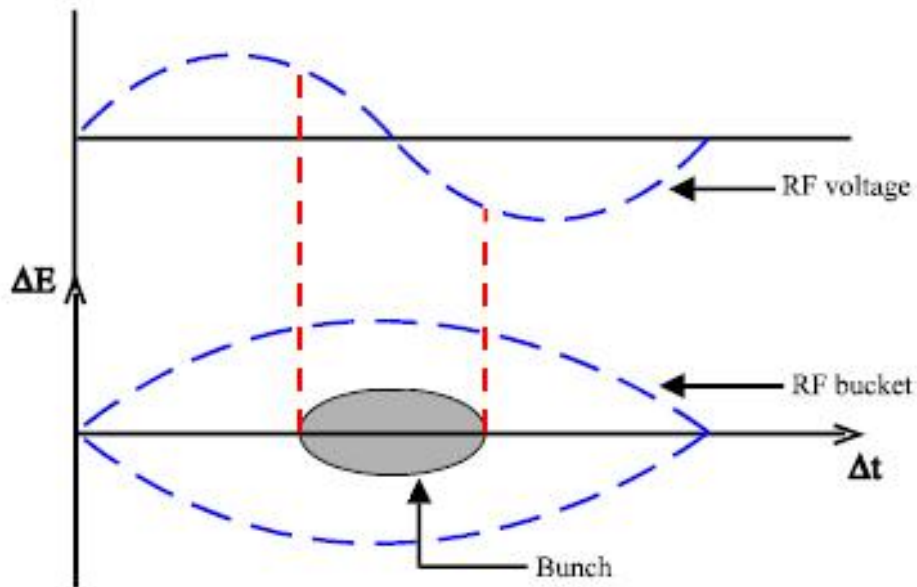
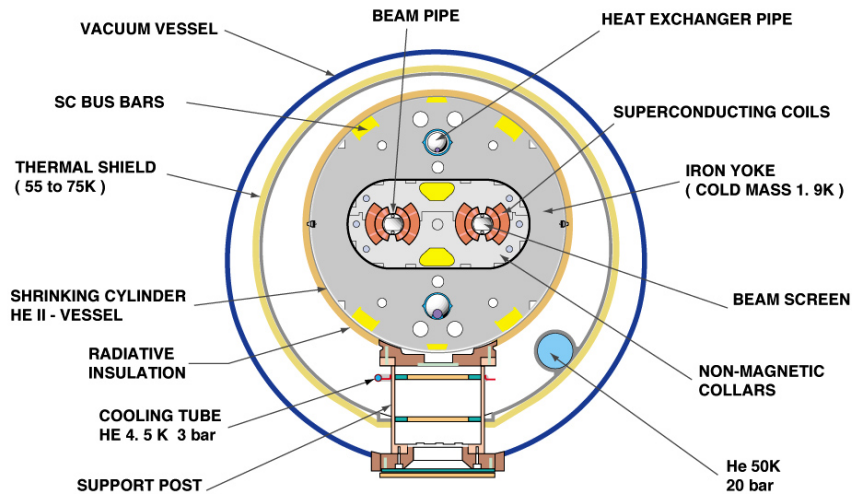


Fig. 3.3: Proton bunch capture onto RF bucket [7].

CROSS SECTION OF LHC DIPOLE



CERN AC _HE107A_ V02/02/98

Fig. 3.4: Cross section of LHC dipole [10]

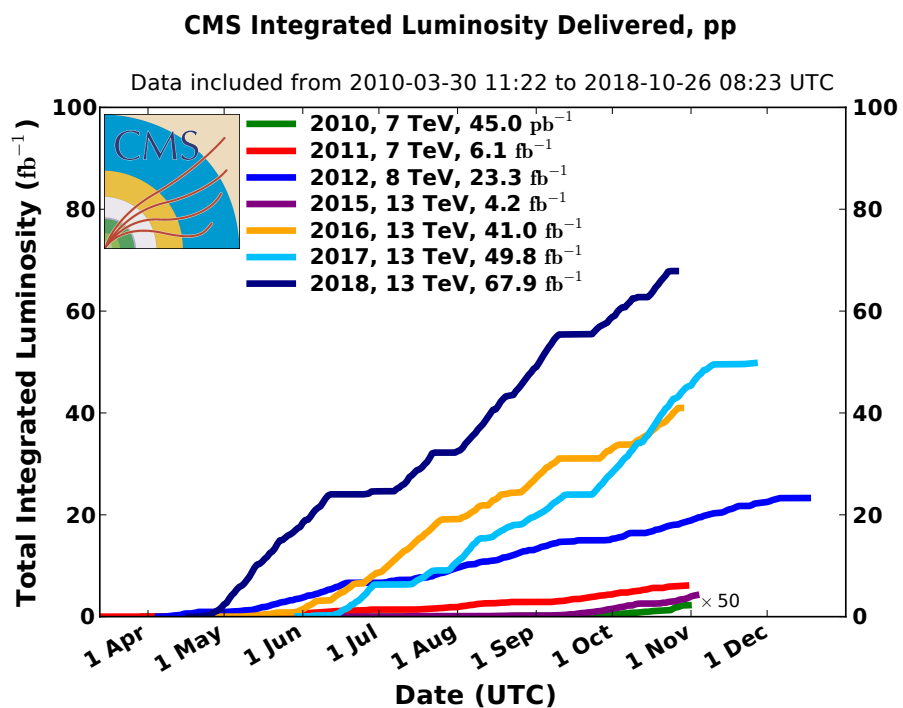


Fig. 3.5: Integrated luminosity delivered by the LHC to the CMS experiment each year from 2010-2018.

120

4. COMPACT MUON SOLENOID

121

4.1 Introduction

122 About 100 meters below the town of Cessy, France at Point 5 is the Compact
 123 Muon Solenoid (CMS). The CMS is a general purpose detector weighing
 124 14,000 tonnes with a length of 28.7 meters and a 15.0-meter diameter that
 125 was designed to accurately measure the energy and momentum of particles
 126 produced in the proton-proton or heavy-ion collisions at the LHC [14]. A
 127 perspective view of the detector is shown in Figure 4.1. In order to get
 128 a full picture of what is being produced by the collisions the CMS detector
 129 must be able identify the resulting particles as well as accurately measure
 130 their energy and momentum. For this reason the detector was designed to
 131 be a collection of specialized sub-detectors, each of which contributes data
 132 used in the reconstruction of a collision.

133 At the heart of the CMS detector is a 3.8-Tesla magnetic field produced
 134 by a superconducting solenoid. Inside the 6-meter diameter solenoid are
 135 three layers of sub-detectors. These make up the inner detector and are, in
 136 order from innermost to outermost, the silicon tracker, the electromagnetic
 137 calorimeter (ECAL), and the hadronic calorimeter (HCAL). Outside the
 138 solenoid is the muon system. A transverse slice of the detector (Figure 4.2)
 139 shows the sub-detectors and how different types of particles interact with
 140 them. Table 4.1 shows a summary of which sub-detectors are expected
 141 to produce signals for different types of particles.

Particle	Tracker	ECAL	HCAL	Muon
Photons	No	Yes	No	No
Electrons	Yes	Yes	No	No
Hadrons (charged)	Yes	Yes	Yes	No
Hadrons (neutral)	No	No	Yes	No
Muons	Yes	Yes	Yes	Yes
Invisible (ν , SUSY, etc)	No	No	No	No

Tab. 4.1: Summary of signals expected for each particle type in each sub-detector.

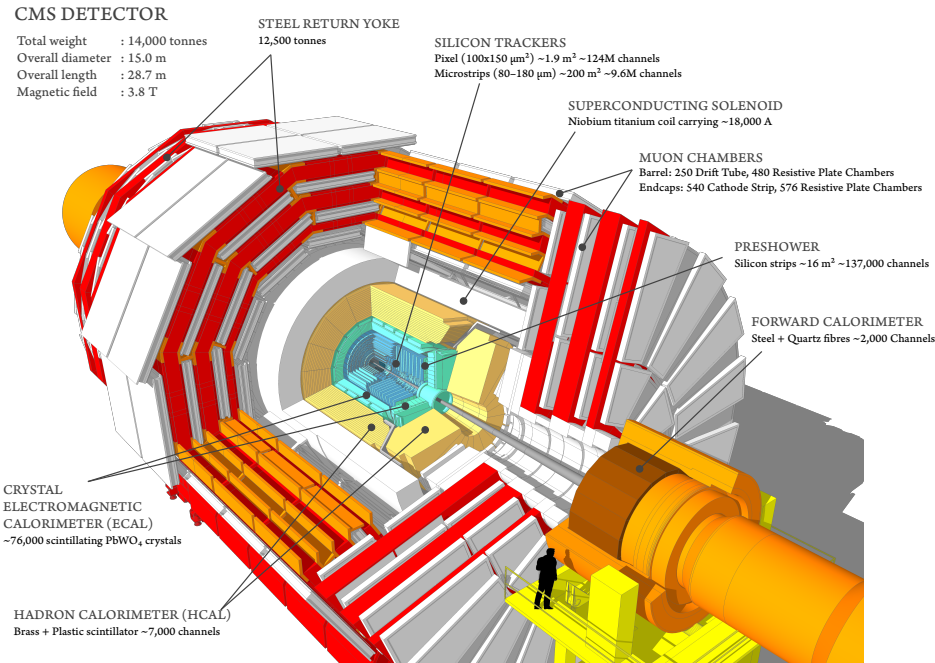


Fig. 4.1: Schematic of CMS detector [25]

142

4.2 Coordinate System

The origin of the coordinate system used by CMS is centered at the nominal collision point in the center of the detector. A right-handed Cartesian system is used with the x-axis pointing radially inward toward the center of the LHC ring, y-axis pointing vertically upward, and the z-axis pointing tangent to the LHC ring in the counterclockwise direction as viewed from above. CMS also uses an approximately Lorentz invariant spherical coordinate system spanned by three basis vectors. They are the transverse momentum p_T , pseudorapidity η , and azimuthal angle ϕ . The transverse momentum and azimuthal angle translate to the Cartesian system in the following ways using the x and y-components of the linear momentum:

$$p_T = \sqrt{(p_x)^2 + (p_y)^2} \quad (4.1)$$

$$\phi = \tan^{-1} \frac{p_y}{p_x} \quad (4.2)$$

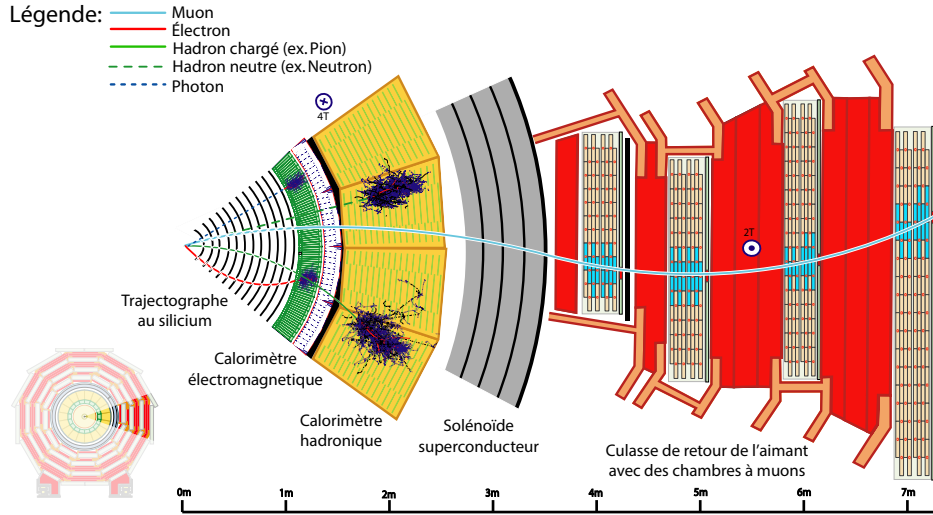


Fig. 4.2: Transverse slice of the CMS detector[8].

while the pseudorapidity can be translated using the polar angle θ relative the positive z-axis as

$$\eta = -\ln[\tan \frac{\theta}{2}]. \quad (4.3)$$

143

4.3 Tracker

144 The innermost sub-detector in CMS is the silicon tracker. The tracker is
 145 used to reconstruct tracks and vertices of charged particles. In order to give
 146 precise reconstruction of charged particle trajectories it needs to be position
 147 as close as possible to the IP and have high granularity. The close proximity
 148 to the IP requires the materials to be tolerant to the high levels of radiation
 149 in that region. Being the innermost sub-detector it must also minimally
 150 disturb particles as they pass through it into the other sub-detectors. These
 151 criteria led to the design of the tracker using silicon semiconductors.

152 The silicon tracker is made up of two subsystems, an inner pixel detector
 153 and an outer strip tracker which are oriented in a cylindrical shape with an
 154 overall diameter of 2.4 m and length of 5.6 m centered on the interaction
 155 point. Both subsystems consist of barrel and endcap regions which can be
 156 seen in Figure 4.3.

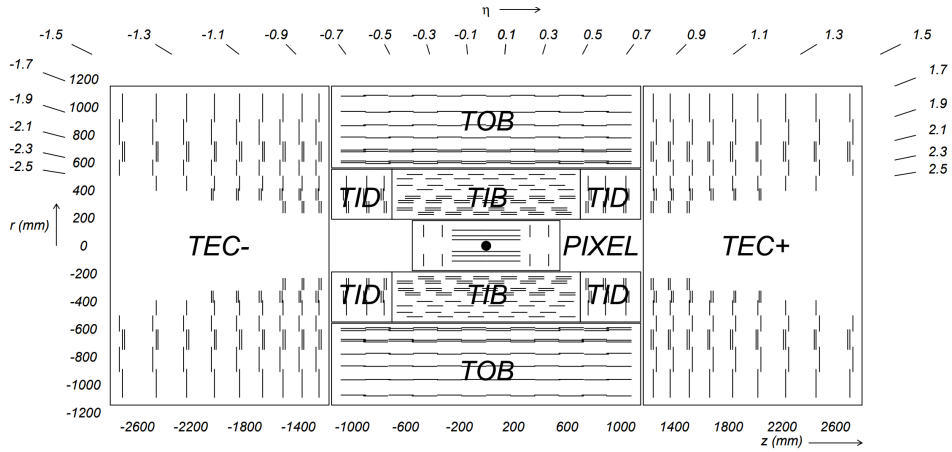


Fig. 4.3: Cross section (side) of CMS tracker prior to the Phase 1 upgrade during the year-end technical stop of 2016/2017. Each line represents a detector module while double lines indicate back-to-back strip modules. Surrounding the pixel tracker (PIXEL) is the strip detector, which is divided into the Tracker Inner Barrel (TIB), Tracker Outer Barrel (TOB), Tracker Inner Disks (TID), and Tracker Endcaps (TEC). Reprinted from Reference [13].

157

4.3.1 Pixel Detector

158 The pixel detector is the innermost subsystem in the silicon tracker and
 159 spans the pseudorapidity range $|\eta| < 2.5$ and is responsible for small im-
 160 pact parameter resolution which is important for accurate reconstruction of
 161 secondary vertices [14]. In order to produce these precise measurements a
 162 very high granularity is required. In addition to this the proximity to the
 163 IP means that one expects there to be high occupancy of the tracker. These
 164 constraints are met by using pixels with a cell size of $100 \times 150 \mu\text{m}^2$.

165 The original pixel detector was designed for operation at the nominal
 166 instantaneous luminosity of $10^{34} \text{ cm}^{-2}\text{s}^{-1}$ with 25 ns between proton bunch
 167 crossings, resulting in on average about 25 proton-proton interactions occur-
 168 ring per bunch crossing or pileup [13]. During the LHC technical shutdown
 169 of 2016/17, the pixel detector underwent the scheduled Phase 1 upgrade
 170 which would allow operation at higher levels of instantaneous luminosity
 171 and pileup. Figure 4.4 shows a cross sectional view in the r - z plane. Prior
 172 to 2017 there were three barrel layers and two endcap layers on each side
 173 which provide three very precise space points for each charged particle. The
 174 upgrade decreased the radius of the innermost barrel layer from 4.4 cm to

3.0 cm and added a fourth barrel layer as well as adding third endcap layer to each side. Each of the endcap layers consisted of two half-disks populated with pixel modules whereas the upgraded endcap layers were split into inner and outer rings. [12]

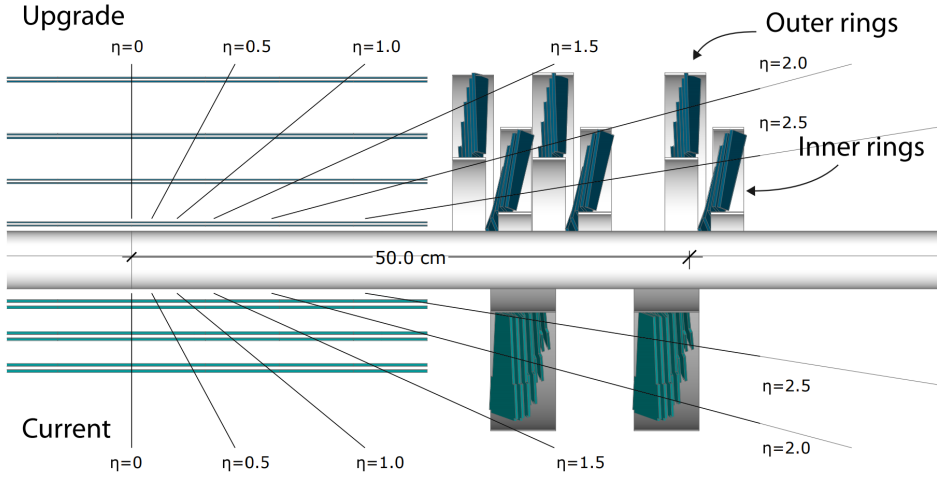


Fig. 4.4: Cross section (side) of pixel detector. The lower half , labeled "Current", shows the design prior to 2017 while the upper half, labeled "Upgrade", shows the design after the upgrade. Reprinted from Resource [12]

179

4.3.2 Strip Detector

180 The silicon strip detector surrounds the pixel detector and is comprised of
 181 four subsystems, the Tracker Inner Barrel (TIB), the Tracker Outer Barrel
 182 (TOB), the Tracker Inner Disks (TID), and the Tracker Endcaps (TEC),
 183 all of which can be seen in Figure 4.3 [14]. The TIB and TID both use
 184 320 μm thick silicon micro-strip sensors oriented along z and r respectively.
 185 The TIB has four layers while the TID is composed of three layers. This
 186 geometry allows the TIB and TID to combine to provide up to four $r - \phi$
 187 measurements on charged particle trajectories.

188 Surrounding the TIB and TID is the TOB, which extends between $z \pm 118$
 189 cm. This subsystem consists of six layers of 500 μm thick silicon micro-strip
 190 sensors with strip pitches ranging from 122 μm to 183 μm , providing six
 191 more $r - \phi$ measurements in addition to those from the TIB/TID subsystems.
 192 Beyond the z range of the TOB is the TEC. Each TEC is made up of nine
 193 disks. Each of the nine disks has up to seven concentric rings of micro-strip
 194 sensors oriented in radial strips with those on the inner four rings being

195 320 μm thick and the rest being 500 μm thick, providing up to nine ϕ
 196 measurements for the trajectory of a charged particle.

197 To provide additional measurements of the z coordinate in the barrel and
 198 r coordinate in the disks a second micro-strip detector module is mounted
 199 back-to-back with stereo angle 100 mrad in the first two layers of the TIB
 200 and TOB, the first two rings of the TID, and rings 1, 2, and 5 of the TEC.
 201 The resulting single point resolution is 230 μm in the TIB and 530 μm in the
 202 TOB. The layout of these subsystems ensures at least nine hits for $|\eta| < 2.4$
 203 with at least four of hits yielding a 2D measurement.

204 4.4 Electromagnetic Calorimeter

205 The electromagnetic calorimeter (ECAL) lies just outside the tracker and is a
 206 hermetic homogeneous calorimeter designed to measure the energy deposited
 207 by electrons and photons. It consists of a central barrel (EB) with 61200
 208 lead tungstate (PbWO_4) crystals which is closed by two endcaps (EE), each
 209 having 7324 crystals. Highly-relativistic charged particles passing through a
 210 crystal primarily lose energy by producing bremsstrahlung photons. Photons
 211 lose energy by producing $e^- - e^+$ pairs. In front of each EE is a preshower
 212 (ES) detector which acts as a two-layered sampling calorimeter. The crystals
 213 in the EB are instrumented with avalanche photodiodes (APDs) while the
 214 EE crystals are instrumented with vacuum phototriodes (VPTs). The ECAL
 215 design was strongly driven to be sensitive to the di-photon decay channel
 216 of the Higgs boson. This led to the design of a calorimeter that was fast,
 217 radiation-hard, and had good spatial and energy resolution.

218 4.4.1 Crystals

219 In order to provide a good spacial resolution it was necessary for the ECAL
 220 to have a fine granularity. The small Molier radius (22 mm) and short radia-
 221 tion length (8.9 mm) of PbWO_4 allows for fine granularity while maintaining
 222 good energy resolution by containing nearly all of the energy from an EM
 223 shower without the need for a restrictively thick crystal layer. The PbWO_4
 224 scintillation is also fast enough that approximately 80 percent of an EM
 225 shower is produced within 25 ns, which is the also the amount of time be-
 226 tween bunch crossings at the LHC. These crystals have a Gaussian-shaped
 227 spectrum spanning from 360 nm to 570 nm with a maximum at approx-
 228 imately 440 nm. While PbWO_4 is relatively radiation-hard, the amount
 229 of ionizing radiation seen by the crystal leading up to the HL-LHC era of
 230 operations causes wavelength-dependent degradation in light transmission.

231 The scintillation mechanism however is unchanged so this damage can be
 232 tracked and accounted for by injecting laser light near the peak wavelength
 233 of the emission spectrum into the crystals to monitor optical transparency.

234 Light produced in the crystal is transmitted along its length and col-
 235 lected at the rear by either an APD in the EB or a VPT in one of the EE.
 236 Light output is temperature dependent so the crystals are kept at precisely
 237 18°C at which the yield is about 4.5 photoelectrons per MeV. The EB and
 238 EE crystals, which have a tuncated pyramidal shape to match the lateral de-
 239 velopment of the shower, along with their photosensors are shown in Figure
 240 4.5.

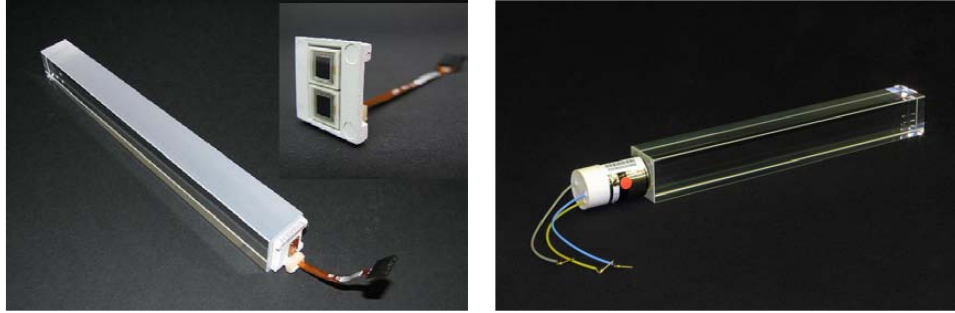


Fig. 4.5: PbWO₄ crystals. Left: EB crystal with APD. Right: EE crystal with VPT. Reprinted from [14]

241

4.4.2 Barrel and Endcaps

242 The EB covers the pseudorapidity range $|\eta| < 1.479$ and uses crystals that
 243 are 230 mm long, which corresponds to 25.8 radiation lengths. The front
 244 face of each crystal measures $22 \times 22 \text{ mm}^2$ while the rear face measures 26×26
 245 mm^2 . These are grouped in 36 supermodules (SM), each comprised of 1700
 246 crystals arranged in a 20×85 grid in $\phi \times \eta$. Each SM spans half the length
 247 of the barrel and covers 20° in ϕ . On the back face of each crystal is a
 248 pair of APDs (semiconductor diodes). APDs are compact, immune to the
 249 longitudinal 3.8 T magnetic field produced by the solenoid at this location,
 250 and resistant to the radiation levels expected in the EB over a ten year
 251 period. They also have high enough gain to counter to low light yield of
 252 the crystals. All of this makes them an ideal choice for use in the EB. Each
 253 APD has an active area of $5 \times 5 \text{ mm}^2$ and are operated at a gain of 50 which
 254 requires a bias voltage between 340 and 430 V. As the gain of the APDs is
 255 highly dependent on the applied bias voltage and any gain instability would

translate to degradation in energy resolution, very stable power supplies are used to maintain voltages within a few tens of mV.

The EE cover the pseudorapidity range $1.497 < |\eta| < 3.0$. The crystals in the EE have a $28.62 \times 28.62 \text{ mm}^2$ front face cross section and $30 \times 30 \text{ mm}^2$ rear face cross section. Each crystal is 220 mm long which corresponds to 24.7 radiation lengths and are grouped in 5×5 units called supercrystals (SCs). Two halves, called *Dees*, make up each EE. Each Dee contains 138 SCs and 18 partial SCs which lie along the inner and outer circumference. On the back of each crystal in EE is a VPT which is a conventional photomultiplier with a single gain stage. While not as compact as the APDs used in the EB, the VPTs are a more suitable for the more hostile environment at higher η . Each VPT has a 25-mm diameter and approximately 280 mm^2 of active area. Though the VPT gain and quantum efficiency are lower than that of the APDs this is offset by the larger active area allowing for better light collection. Figure 4.6 shows the orientation of the crystals, modules, and supermodules within the ECAL. [14]

4.4.3 Preshower layer

In front of each EE is a preshower (ES) detector. The main purpose of the ES is to identify photons resulting from $\pi^0 \rightarrow \gamma\gamma$ within the pseudorapidity range $1.653 < |\eta| < 2.6$, but it also aids in the identification of electrons against minimum ionizing particles (MIPs) and provides a spacial resolution of 2 mm compared to the 3 mm resolution of the EB and EE. The ES acts as a two-layered sampling calorimeter. Lead radiators make up the first layer. These initiate electromagnetic showers from incoming electrons or photons. The deposited energy and transverse profiles of these showers are then measured by the silicon strip sensors which make up the second layer.

4.4.4 Performance

The energy resolution of the ECAL can be parameterized as

$$\frac{\sigma}{E} = \frac{S}{\sqrt{E}} \oplus \frac{N}{E} \oplus C \quad (4.4)$$

where S is the stochastic term characterizing the size of photostatistical fluctuations, N is the term characterizing the contributions of electronic, digital, and pileup noise, and C is a constant which accounts for crystal performance non-uniformity, intercalibration errors, and leakage of energy from the back of a crystal. The values for these terms, as measured in a

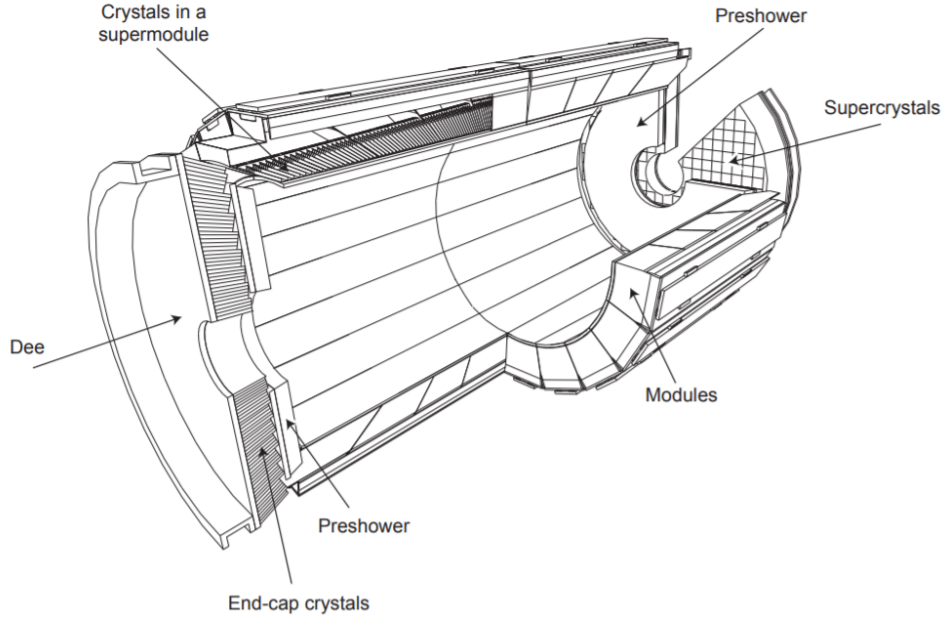


Fig. 4.6: Schematic of ECAL. Reprint from [14]

beam test using 20 to 250 GeV electrons, are $S = 0.028 \text{ GeV}^{1/2}$, $N = 0.12$ GeV, and $C = 0.003$. [14]

4.5 Hadronic Calorimeter

In the space between the bore of the superconducting magnet and the ECAL is the Hadronic Calorimeter (HCAL) [2]. The HCAL is a sampling calorimeter used for the measurement of hadronic jets and apparent missing transverse energy resulting from neutrinos or exotic particles. It is made up of alternating layers of plastic scintillator tiles and brass absorbers. EM showers are generated by charged/neutral hadrons in the brass absorber. Charged particles in the shower then produce scintillation light in the plastic scintillator. Wavelength-shifting optical fibers embedded in the scintillator collect and guide the scintillation light to pixelated hybrid photodiodes. A longitudinal cross-section view in Figure 4.7 shows the geometric layout of the HCAL's barrel (HB), outer barrel (HO), endcap (HE), and forward (HF) sections. The HB is comprised of 17 scintillator layers extending from 1.77 to 1.95 m and covers the pseudorapidity range of $|\eta| < 1.4$. The HO lies outside the solenoid and is composed of only scintillating material. This

increases the interaction depth of the calorimeter system to a minimum of $11\lambda_I$ for $|\eta| < 1.26$ and thus reduces energy leakage. Also located inside the solenoid are the two HE which cover pseudorapidities $1.3 < |\eta| < 3.0$ and provide a thickness of $10\lambda_I$. In the forward region is the HF. This is located 11.2 m away from the IP and covers the $2.9 < |\eta| < 5.2$. As the HF is exposed to the highest levels of particle flux, it uses quartz fibers embedded in steel absorbers rather than the materials used in the other parts of the HCAL. Showers initiated by the absorbers produce Cerenkov light in the quartz which transmits along to the fibers to photomultiplier tubes (PMTs).

The HCAL inherently has lower energy resolution than the ECAL. A large portion of the energy from hadronic showers is deposited in the absorbers and never makes it to the scintillation material. There are also the possibilities that showers can be initiated prior to the particles reaching HCAL or a charged particle could deposit energy in the ECAL through bremsstrahlung. The combined energy resolution of the ECAL and the HCAL barrels can be parameterized as

$$\frac{\sigma}{E} = \frac{S}{\sqrt{E}} \oplus C, \quad (4.5)$$

where E is the energy of the incident particle. These quantities were measured in a beam test using 2 to 350 GeV/c hadrons, electrons, and muons. The stochastic term is $S = 0.847 \text{ GeV}^{1/2}$, and the constant term is $C = 0.074$ [4].

4.6 Superconducting Solenoid

In between the HCAL barrel and outer barrel is the superconducting solenoid magnet. The magnet is 12 m long with a 6-m inner diameter and provides the bending power necessary to precisely measure the momentum of charged particles. While it is capable of producing a 4 T magnetic field, the magnet is typically operated at 3.8 T. This is done to prolong the lifetime of the magnet. The Niobium Titanium coils used to create the uniform 3.8-T magnetic field are suspended in a vacuum cryostat and cooled by liquid helium to a temperature of 4.5 K. The magnet has a stored energy of 2.6 GJ when operating at full current. There are five wheels in the barrel and three disks on each endcap that make up a 12,000 ton steel yoke which serves to return the magnetic flux. This, along with a mapping of the calculated field strength, can be seen in Figure 4.8. More details on the superconducting solenoid magnet can be found at [1]

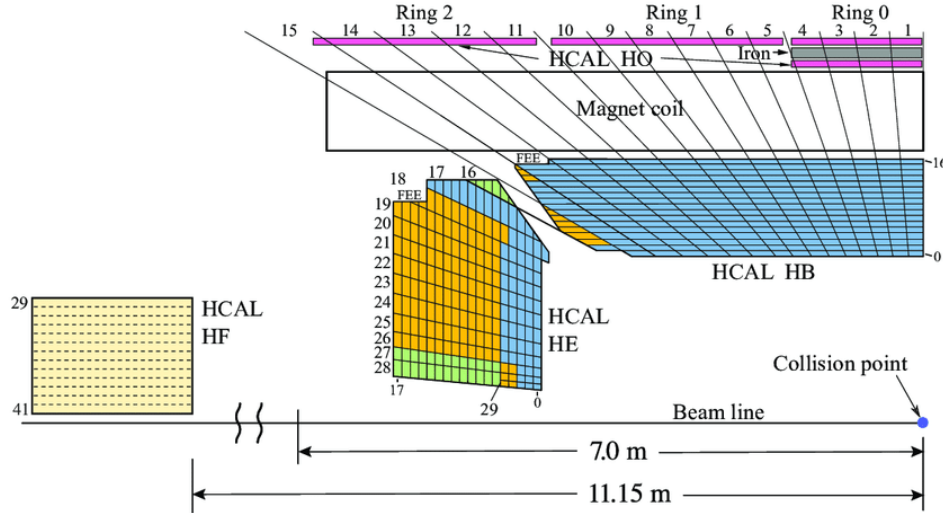


Fig. 4.7: Longitudinal view of HCAL [2]

333 4.7 Muon System

334 Embedded in magnet return yoke and encapsulating all of the other sub-
 335 detectors is the muon system. The muon system is the outermost layer
 336 because muons don't interact via the strong force and electromagnetic in-
 337 teractions alone are not enough stop them due to their large mass, therefore
 338 the only particles that are capable of making it to the muon system are
 339 muons and weakly-interacting particles such as neutrinos. The muon sys-
 340 tem is comprised of three different types of detectors. These are drift tube
 341 (DT) chambers, cathode strip chambers (CSC), and resistive plate chambers
 342 (RPC). A cross-sectional view of the muon system along with the rest of the
 343 CMS detector is shown in Figure 4.9.

344 The DT chambers are used barrel region for $|\eta| < 1.2$. Each chamber is
 345 comprised of three superlayers which are made up of four staggered layers
 346 of rectangular drift cells. Each of these drift cells contains a mixture of
 347 Ar and CO₂ gases. An anode wire, located at the center of each tube, is
 348 made of gold-plated stainless steel and is held at 3.6 kV. The gas is ionized
 349 when a charged particle passes through and the resulting free electrons are
 350 attracted to the anode wire. As these electrons pass through the gas they
 351 cause further ionization which results in an electron avalanche. The layers
 352 of drift cells are oriented in such a way that two of the three superlayers
 353 give the muon position in the ϕ -direction and one gives the position in the

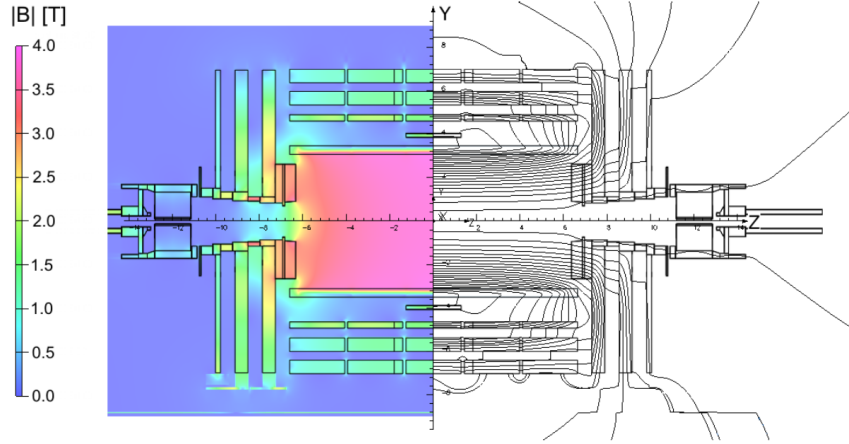


Fig. 4.8: Longitudinal slice of CMS detector while operating at 3.8-T central magnetic field. The right-hand side of the figure shows a mapping of the magnetic field lines while the left-hand side shows a mapping of the field strength. Reprint from [11]

354 z -direction. The result is a spacial resolution of 77-123 μm along the ϕ
 355 direction and 133-193 μm along the z direction for each DT chamber [15].

356 On the endcaps, covering the pseudorapidity range of $0.9 < |\eta| < 2.4$,
 357 are the CSCs. In this region there is a higher muon flux as well non-uniform
 358 magnetic fields so this portion of the muon system must have higher gran-
 359 ularity provided by the CSCs. Each of these chambers contain panels that
 360 divide it into six staggered layers. The cathode strips are oriented along the
 361 r -direction to give position measurements in the ϕ -direction while anode
 362 wires run perpendicular in between the panels to give r -direction position
 363 measurements. The spacial resolution provided by the CSCs is 45-143 μm
 364 [27].

365 Both the endcap and barrel regions, spanning $|\eta| < 1.6$, contain RPCs to
 366 provide more precise timing measurements. Each RPC is a gaseous parallel-
 367 plate detector. High voltage is applied to two large plates which have a
 368 layer of gas between them. Outside the chamber is an array of cathode
 369 strips which is used to detect electron cascades resulting from muons passing
 370 through and ionizing the gas. Where the DTs and CSCs provide precise
 371 position information, the RPCs have a very fast response time which gives
 372 a time resolution better than 3 ns [27]. This allows for the RPCs to be used
 373 as a dedicated muon trigger that can insure each muon is assigned to the
 374 correct bunch crossing.

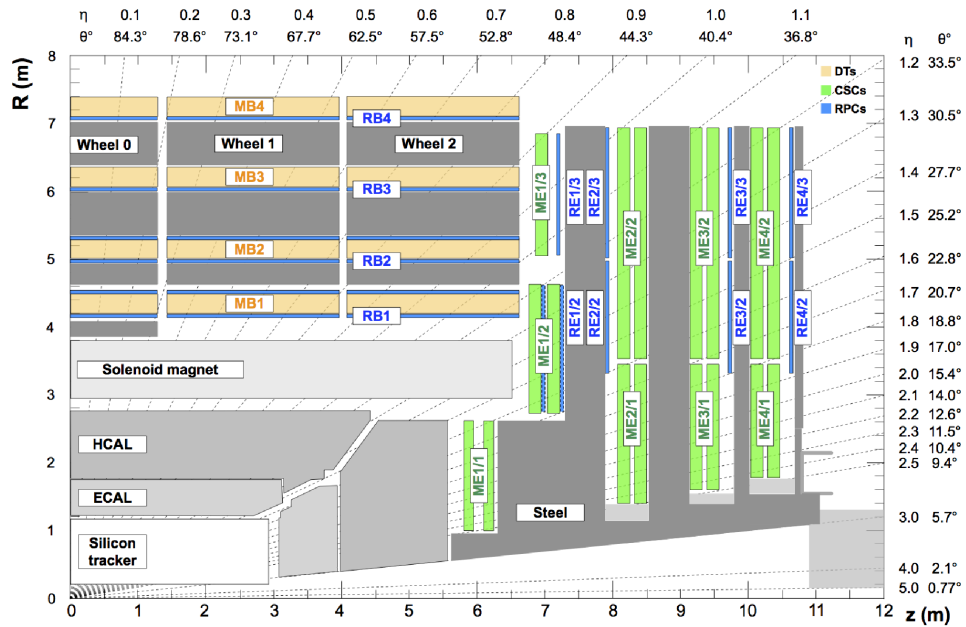


Fig. 4.9: Cross-section of one quadrant of the CMS detector. The DTs are labeled as "MB" (Muon Barrel) and the CSCs are labelled as "ME" (Muon Endcap). The RPCs are "RB" for those in the barrel and "RE" for those in the endcap. Reprint from [27].

375

5. MIP TIMING DETECTOR (MTD)

376

5.1 Introduction

377 In the coming years the LHC will be working toward upgrades that will
 378 lead a substantial increase in luminosity. The timeline for future operations
 379 of the LHC is shown in Figure 5.1. In 2019 the LHC entered a two-year
 380 shutdown, Long Shutdown 2 (LS2). Upgrades of the LHC injector complex
 381 to increase the beam brightness will take place during this shutdown. After
 382 LS2 the LHC will enter Run 3 which will run for three years at 13-14 TeV. At
 383 the completion of Run 3 the LHC will enter Long Shutdown 3 (LS3) which
 384 will last approximately 2.5 years. During LS3 the optics in the interaction
 385 region will be upgraded to produce smaller beams at the interaction point.
 386 The completion of this upgrade will usher in the High Luminosity (HL-LHC)
 387 era or Phase 2 of LHC operations, during which the combination of brighter
 388 beams and a new focusing scheme at the IP allows for a potential luminosity
 389 of $2 \times 10^{35} \text{ cm}^{-2}\text{s}^{-1}$ at the beginning of each fill [6].

LHC/ High-Luminosity LHC timeline



Fig. 5.1: Timeline for LHC [16]

390 The increased luminosity results in more interactions per bunch crossing
 391 or pileup. In order to limit the amount of pileup the experiments must
 392 disentangle to more manageable levels, the nominal scenario would be op-

erating at a stable luminosity of $5.0 \times 10^{34} \text{ cm}^{-2} \text{ s}^{-1}$. This would limit the pileup to an average of 140. The ultimate scenario for operations would be running at $7.5 \times 10^{34} \text{ cm}^{-2} \text{ s}^{-1}$ which brings the average pileup up to 200. The CMS detector in its current state is not capable of dealing with $\approx 140\text{-}200$ pileup. At this level of pileup the spacial overlaps of tracks and energy depositions would lead to a degradation in the ability to identify and reconstruct hard interactions. In order to preserve the data quality of the current CMS detector this increased pileup must be reduced to an equivalent level approximately equal to current LHC operations which is ~ 40 . The collision vertices within a bunch crossing have an RMS spread of 180-200 ps in time. If the beam spot were to be sliced into consecutive snap shots of 30-40 ps then the pileup levels per snapshot would be approximately 40. The space-time reconstruction of a 200 pileup event is shown in Figure ???. The addition of timing information to the z position spreads apart the vertices that would otherwise have been merged together and indiscernible. In order to achieve this a detector dedicated to the precise timing of minimum ionizing particles (MIPs), the MTD, will be added to the CMS detector.

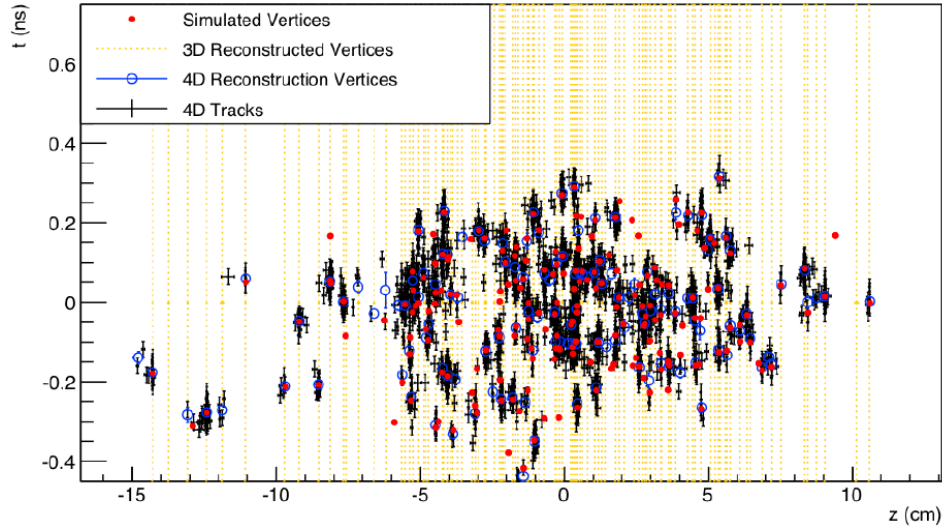


Fig. 5.2: Vertices from a simulated 200 pileup event with MTD timing resolution of ~ 30 ps. The red dots represent the simulated vertices while the yellow lines indicate vertices reconstructed without the use of timing information. The black crosses and blue open circles represent tracks and vertices reconstructed using time information from the MTD. Reprint from

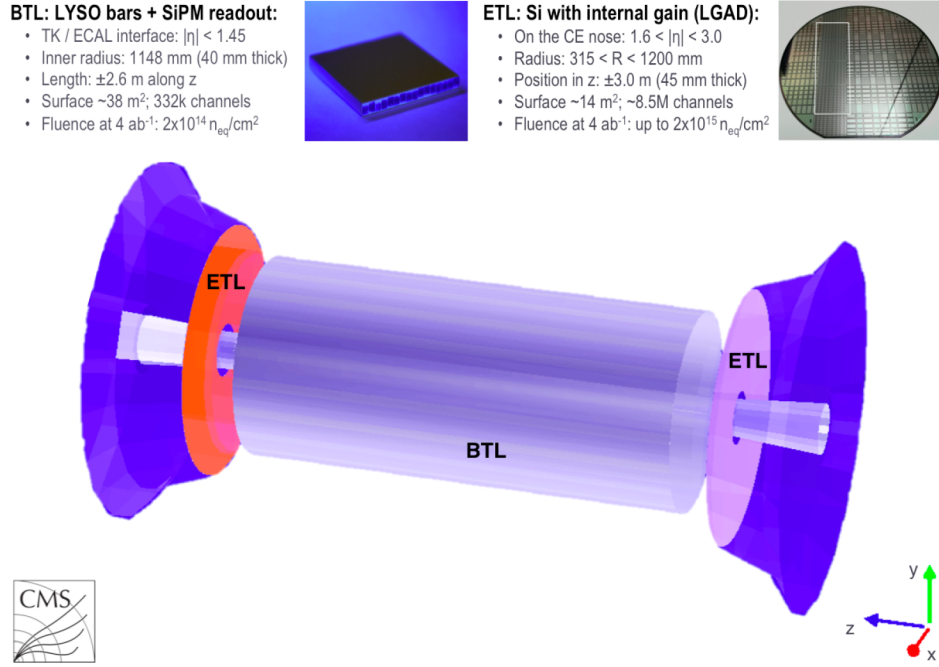


Fig. 5.3: Schematic view of the proposed MTD implemented in the GEANT simulation of the CMS detector. The central region makes up the BTL which will be located in the space between the tracker and the ECAL. The ETL will be located in front of the endcap calorimeter. Reprint from

410

5.2 Barrel Timing Layer

411 The Barrel Timing Layer (BTL) makes up the barrel region of the MTD.
 412 It will provide pseudorapidity coverage up to $|\eta| = 1.48$ with a geometric
 413 acceptance of $\sim 90\%$. The BTL will be capable of detecting MIPs with a
 414 time resolution of 30 ps at the start of Phase-2 operations and a luminosity-
 415 weighted time resolution of ~ 45 ps when radiation damage effects are taken
 416 into account. The BTL is designed to operate without significant perfor-
 417 mance degradation over an integrated luminosity of at least 3000 fb^{-1} . The
 418 predicted level of radiation exposure over that integrated luminosity is listed
 419 in Table 5.1.

420 The fundamental element for MIP detection in the BTL is a thin scin-
 421 tillating bar made of Lutetium Yttrium Orthosilicate crystals doped with
 422 Cerium ($(Lu_{1-X}Y_X)_2SiO_5 : Ce$) which is referred to as LYSO:Ce. The bars
 423 are 57 mm long, 3.12 mm wide, and have an average thickness of 3 mm. A

Tab. 5.1: Predicted radiation doses and fluences at different location of the BTL after an integrated luminosity of 3000 fb^{-1} . The two far right columns include a safety margin of 1.5.

$ \eta $	r (cm)	z (cm)	3000 fb^{-1}		$1.5 \times 3000 \text{ fb}^{-1}$	
			n_{eq}/cm^2	Dose (kGy)	n_{eq}/cm^2	Dose (kGy)
0.0	116	0	1.65×10^{14}	18	2.48×10^{14}	27
1.15	116	170	1.80×10^{14}	25	2.70×10^{14}	38
1.45	116	240	1.90×10^{14}	32	2.85×10^{14}	48

424 silicon photomultiplier (SiPM) is attached to each end of the LYSO:Ce bar.
 425 This double-ended readout gives uniform time response along the length of
 426 the crystal by eliminating the time delay effect from light propagating along
 427 the crystal and the ability to extract positional information for tracking.

428 An overview of the BTL and its components is shown in Figure 5.5. The
 429 longitudinal axis of each crystal bar is oriented along the ϕ -direction in the
 430 CMS detector. The crystals are grouped in 1×16 ($\phi \times z$) arrays that each
 431 form a *module*. Each *module* has 32 SiPMs (2 for each bar) resulting in
 432 32 readout channels. These *modules* are then grouped in a 3×8 ($\phi \times z$)
 433 arrangement to make up a readout unit (RU) as shown in Figure 5.6. Each
 434 *module* is read out by a dedicated ASIC called the TOFHIR (Time-of-flight,
 435 High Rate) chip which is capable of reading out 32 channels at a time.
 436 The TOFHIR chip gives precision timing information using discrimination
 437 of the leading edge of pulses from the SiPMs followed by a time-to-digital
 438 converter (TDC). When using discrimination techniques like this the time
 439 for a pulse to cross the discriminating threshold depends on the height of the
 440 pulse. This results in an amplitude-dependent timing variation called time
 441 walk. In order to correct for this time walk effect the ASIC also measures
 442 pulse amplitude. Six ASICs are mounted on each of four front-end boards
 443 (FEBs) on a RU giving a total of 24 ASICs and 768 SiPMs per RU. The
 444 RUs are then arranged in trays along the z -direction. Each tray holds six
 445 RUs, runs along half the length of the detector, and spans 10° along ϕ . To
 446 summarize, a total of 72 trays (36 azimuthal sections each split into a $+z$ and
 447 $-z$ section) contain 331776 SiPMs and 165888 LYSO:Ce bars. This gives
 448 a detector granularity that has an average occupancy of about 7% at 200
 449 pileup, which limits the likelihood of multiple hits within a single crystal
 450 during a bunch crossing.

451 In order to have a negligible impact on the energy resolution of the
 452 ECAL, the thickness of the LYSO:Ce crystals is varied along the z -axis of

the detector. This variation is done in three sections such that the thickness of material is as uniform as possible while not exceeding $0.4 X_0$ where X_0 is one radiation length. This is done in three sections as a function of η where crystal thicknesses of 3.75 mm, 3.0 mm, and 2.4 mm will be in the $|\eta|$ regions 0-0.7, 0.7-1.1, and 1.1-1.48 respectively. These details are outlined in Table 5.2. Figure 5.4 shows how the slant thickness changes along η in terms of radiation length for the case where crystal thicknesses are varied as outlined in Table 5.2.

$ \eta $ range	0-0.7	0.7-1.1	1.1-1.48
Crystal thickness (mm)	3.75	3.0	2.4
Average slant thickness (mm)	4.0	4.3	4.6

Tab. 5.2: Summary of crystal and slant thicknesses in different η regions.

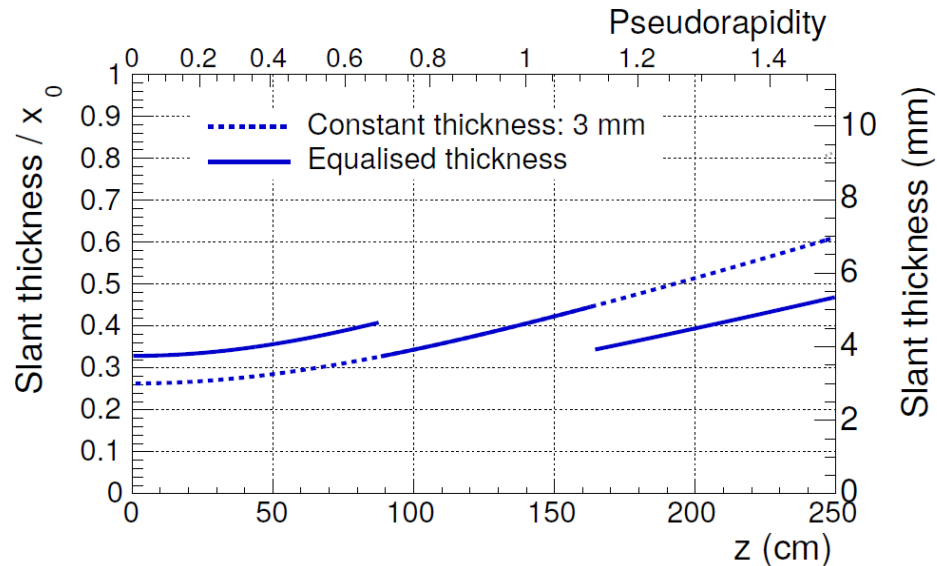


Fig. 5.4: The left and right axes show the slant thickness in terms of radiation length and mm respectively. The dotted blue line shows the slant thickness if all LYSO:Ce bars were 3 mm thick while the solid line has bar thicknesses of 3.75, 3.0, and 2.4 mm. Reprinted from

The "time stamp" provided by the BTL is a measurement of the time that a MIP passes through the volume of a LYSO:Ce crystal it will produce optical photons along its path. The number

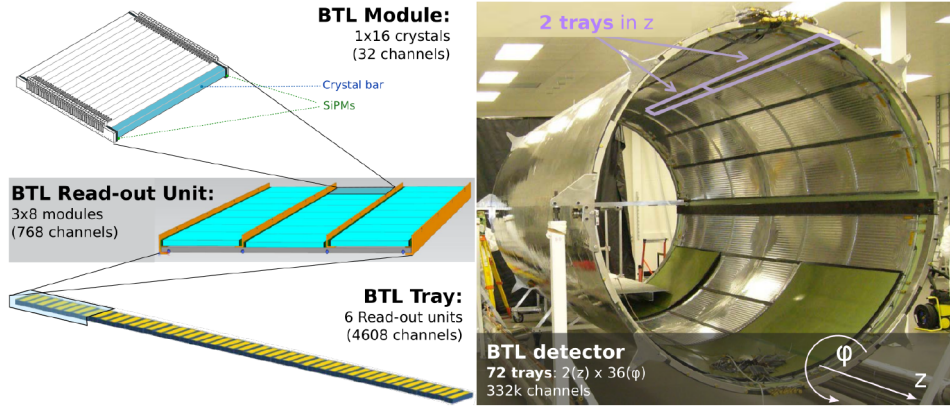


Fig. 5.5: On the left is an overview showing how the various components of the BTL fit together into modules, read-out units, and trays. On the right is a view of how the trays will fit into the Tracker Support Tube (TST)

of photons produced is proportional to the light yield (LY) of the crystal, which is a function of the amount of energy deposited. Of these photons, a fraction of them will reflect along the length of the crystal bar and be detected by one of the two SiPMs mounted on the ends. The SiPMs convert these detected photons into photoelectrons to produce electrical signals which are then processed by the TOFHIR chip to provide the "time stamp" for the MIP. Throughout this process there are multiple contributors to time resolution degradation. The sum of these contributions in quadrature as shown in Equation 5.1 gives the overall time resolution for the BTL.

$$\sigma_t^{BTL} = \sigma_t^{clock} \oplus \sigma_t^{digi} \oplus \sigma_t^{ele} \oplus \sigma_t^{pho} \oplus \sigma_t^{DCR} \quad (5.1)$$

The individual contributions are shown in Table ???. As one can see from this

Source	starting σ_t (ps)	end-of-life (3000 fb^{-1}) σ_t (ps)
Clock jitter	15	15
Digitization	7	7
Electronics	8	8
Photo-statistics	25	30
SiPM dark counts	negligible	50

461

462 table, the two major factors in overall time resolution are photo-statistics
463 and, at the end of life, dark counts or noise from the SiPMs. The evo-
464 lution of timing performance of the BTL as a function of the integrated

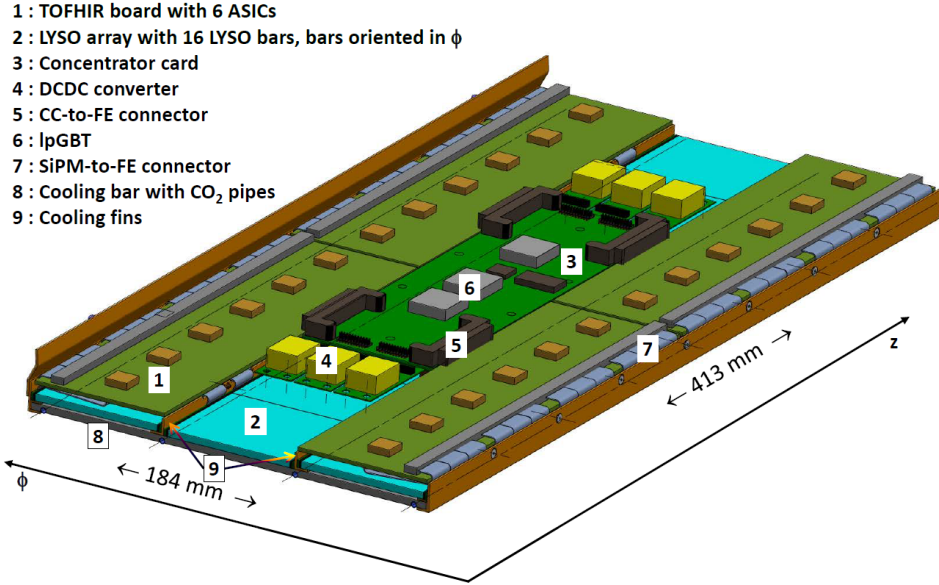


Fig. 5.6: Readout unit for the BTL.

luminosity is shown in Figure 5.7. It's clear that the two most important details required to obtain and preserve good time resolution are optimizing the photo-statistics and mitigating the increased noise produced by heavily irradiated SiPMs as the integrated luminosity approaches the 3000 fb^{-1} end of life target.

5.2.1 LYSO:Ce crystals

As previously stated, photo-statistics has a major impact on the achievable time resolution of the BTL. The contribution to the overall time resolution can be expressed as

$$\sigma_t^{pho} \propto \sqrt{\frac{\tau_r \tau_d}{N_{phe}}} \propto \sqrt{\frac{\tau_r \tau_d}{E_{dep} \times LY \times LCE \times PDE}}, \quad (5.2)$$

where the rise and decay times of the scintillation pulses are τ_r and τ_d respectively, N_{phe} is the number of photoelectrons produced, E_{dep} is the energy deposited in the crystal, LY is the light yield, LCE is the light collection efficiency which is the fraction of optical photons that make it down the length of the crystal to the SiPMs, and PDE is the photon detection efficiency which is the fraction of photons incident on the SiPM surface that

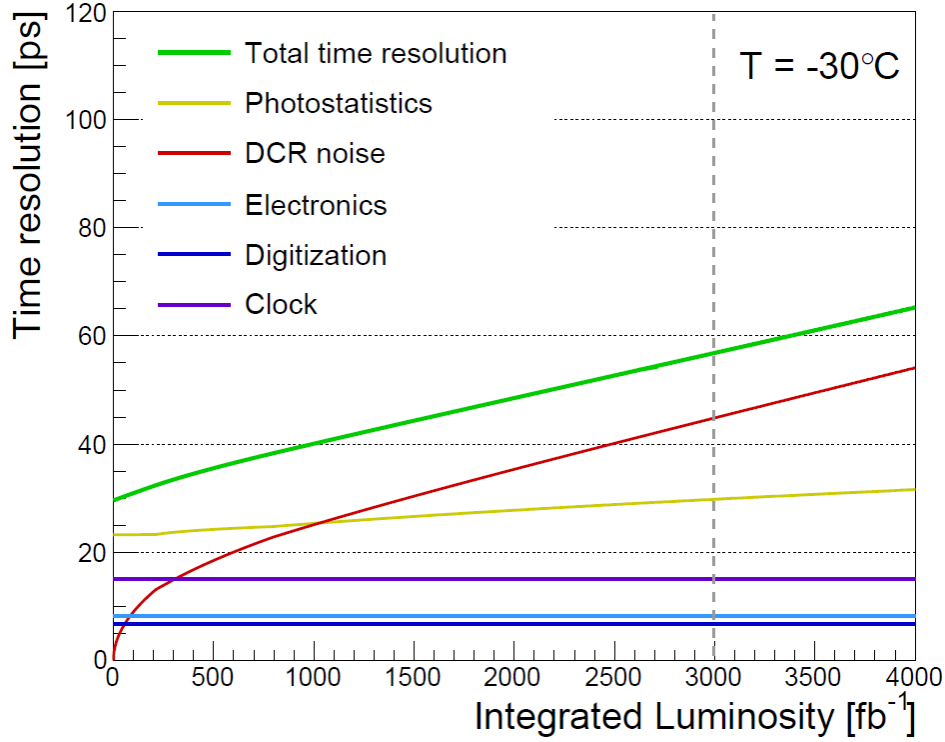


Fig. 5.7: Evolution of time resolution for the BTL.

are detected. From Equation 5.2 we see that an ideal candidate material for the crystals is one with fast decay and rise times, large E_{dep} , and high LY. LYSO:Ce has a decay time ~ 40 ns and a rise time < 100 ps [21]. The energy deposited by a MIP in a crystal follows a Landau distribution with the most probable value being at 0.86 MeV/mm. For the BTL crystals a MIP deposits an average energy of 4.2 MeV when accounting for the longer path lengths within the LYSO:Ce volume due to track bending in the magnetic field. While the LY is about 40000 photons/MeV, the most important photons are the "early photons" which are those produced in the first 500 ps of scintillation. LYSO:Ce produces approximately 400 early photons/MeV resulting in about 2000 early photons being produced per MIP in the BTL.

Additionally, these crystals must be tolerant to radiation levels up to those listed in Table 5.1 with the 1.5 safety margin. Comparing the change in transparency of LYSO:Ce after exposure to 24 GeV proton to a $2.5 \times 10^{13} \text{ cm}^{-2}$ fluence, which is more than the expected level including the

safety margin, show a negligible loss in transparency T (Figure 5.8). At the LYSO:Ce peak scintillation wavelength of 420 nm the induced absorption coefficient is

$$\mu_{ind} = \frac{\ln(T_{before}/T_{after})}{L} = 0.5\text{ m}^{-1} \quad (5.3)$$

where L is the length of the crystal bar. In addition to investigating the

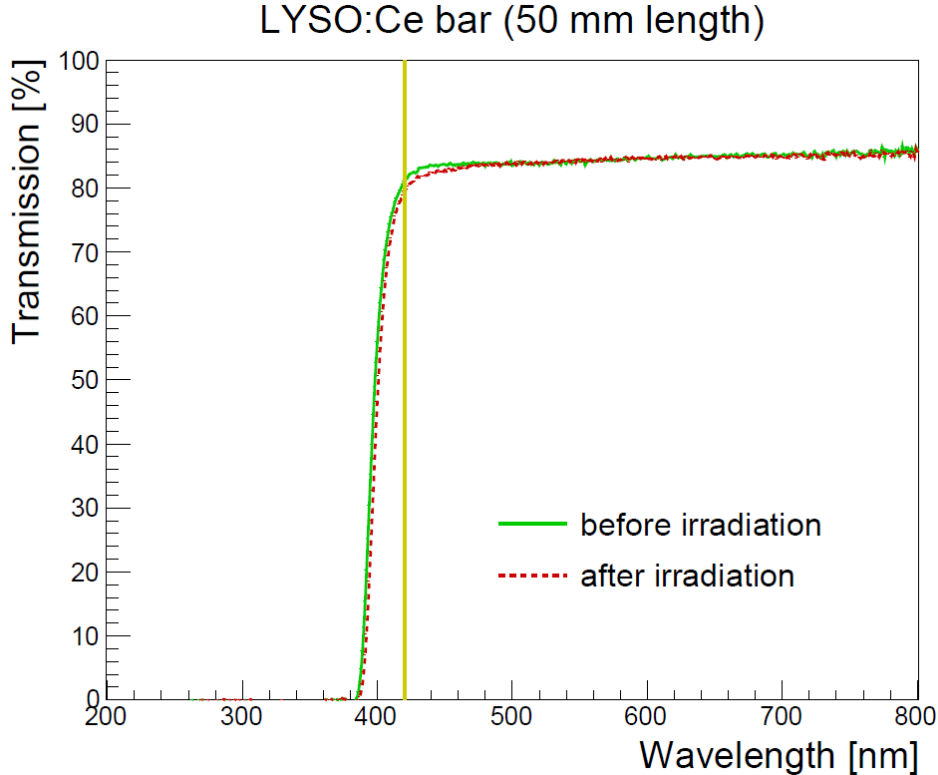


Fig. 5.8: Transmission curve across a 50 mm long bar of LYSO:Ce before and after being irradiated to a fluence of $2 \times 10^{13} \text{ cm}^{-2}$ with 24 GeV protons. The vertical line indicates the peak wavelength in the scintillation emission spectrum of LYSO:Ce.

⁴⁸⁸
⁴⁸⁹ changes in optical transmission, the effect on the timing resolution was also
⁴⁹⁰ checked to insure that the observed changes in the transmission did not
⁴⁹¹ have a substantial effect on the timing performance. The time resolution
⁴⁹² before and after irradiation was measured using 511-keV photons from a
⁴⁹³ Na²² source with the results shown in 5.9. This shows that there is no
⁴⁹⁴ statistically significant change in the time resolution due to the radiation

495 induced changes in optical transmission.

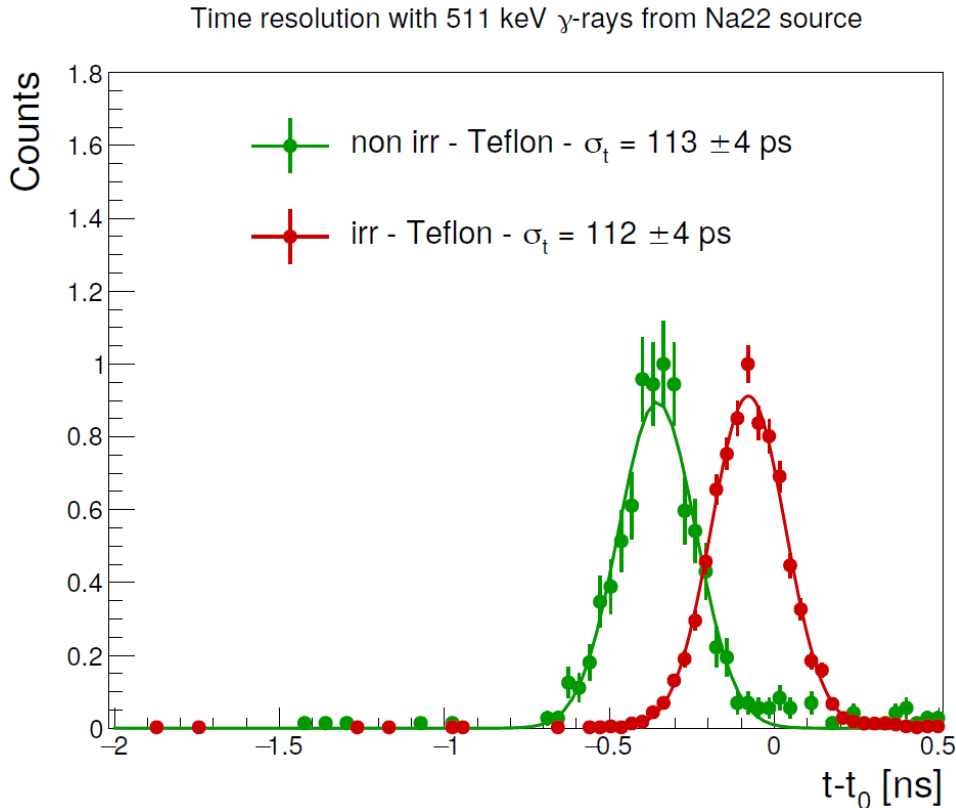


Fig. 5.9: The time resolution of a 50 mm long LYSO:Ce bar was measured before and after being irradiated with 24 GeV protons to a $2 \times 10^{13} \text{ cm}^{-2}$ fluence. The time resolution was measured using 511 keV photons from a Na²² source. There was no significant change in time resolution after being irradiated.

496

5.2.2 SiPMs

497 Silicon photomultiplier (SiPMs) were chosen as the photo-sensor to be used
 498 in the BTL. In contrast to conventional photomultiplier tubes, SiPMs are
 499 compact, robust, and insensitive to external magnetic fields. Several dif-
 500 ferent SiPMs technologies were considered for the BTL. Some important
 501 characteristics to consider are radiation tolerance, photon detection effi-
 502 ciency, power consumption, and timing performance. In consideration were

503 the NUV-HD (thin-epi) SiPM from Fondazione Bruno Kessler (FBK) and
 504 the S12572 and HDR2 SiPMs which are both produced by Hamamatsu Photo-
 505 tonics (HPK). SiPMs with a $15\ \mu\text{m}$ cell size were chosen as it gave the best
 506 balance between radiation tolerance and PDE.

5.2.3 Glue qualification

The LYSO:Ce bars and SiPMs will be coupled together using an optical glue. Preliminary glue candidates were chosen to have an index of refraction similar to that of LYSO:Ce and good optical transmission at the peak wavelength of the LYSO:Ce emission spectrum (420 nm). These candidates were NOA-61, RTV-3145, Epotek, Polytec, BC-600, and Meltmount. Additional constraints were that the glues be mechanically strong, capable of withstanding temperatures ranging from -40 to +60°C, and resistant to an ionizing dose of radiation up to \sim 50 kGy (less than 3% loss in transparency). As Meltmount has a melting temperature below 50°C, it was eliminated from consideration. The remaining glue candidates were tested for radiation hardness using a Cs¹³⁷ irradiator at the University of Virginia Medical Research Facility which provided an ionizing dose at a rate of 2 Gy/min. The primary decay mode for Cs¹³⁷ is a beta decay to an excited state of Ba¹³⁷ which then produces a 662 keV photon when dropping into its ground state. The energy spectrum of for Cs¹³⁷ is shown in Figure 5.10. A preliminary test of radiation tolerance was performed using samples prepared by injecting glue into a teflon mold such as the one shown in Figure 5.11a. Once cured, the glue samples (Figure 5.11b) were removed from the mold and placed in the Cs¹³⁷ irradiator. The received ionizing dose was calculated by multiplying the total time of exposure by the rate of 2 Gy/min. The results, shown in Figure 5.12, narrowed the list of candidates down to NOA-61 and RTV-3145.

At this point a more precise examination of the radiation tolerances for NOA-61 and RTV-3145 were carried out by monitoring transmission properties before and after several subsequent exposures until reaching the integrated ionizing dose of about 50 kGy. Transmission measurements were taken using a photo-spectrometer which directs a beam of light with known wavelength through a sample and into a photo-sensor. In order to minimize optical effects not related to radiation damage the samples need to have uniform thickness and surfaces that are both smooth and parallel. To accomplish this the glue samples for this test were prepared by placing glue between two 1-mm thick quartz tiles which were separated by 1-mm thick spacers. The quartz provided smooth surfaces while the spacers insured

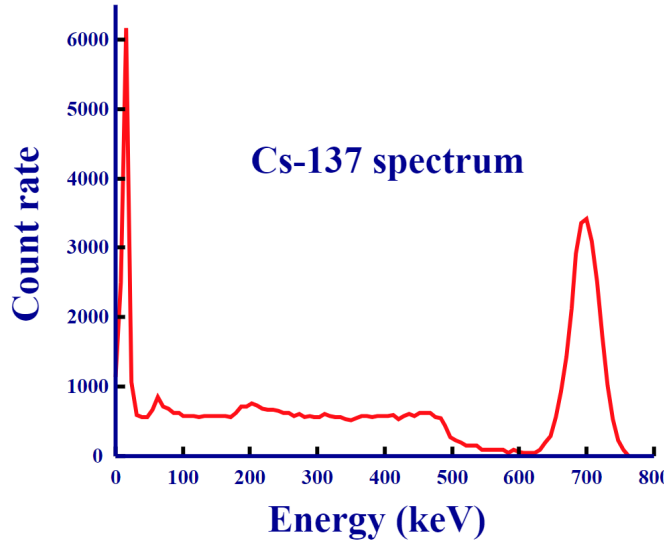


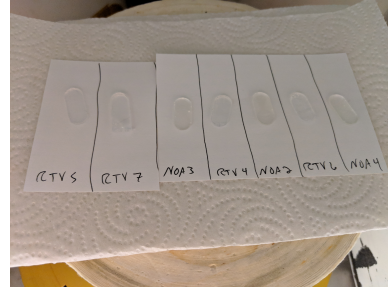
Fig. 5.10: Energy spectrum for Cs^{137} .

541 uniform glue thicknesses and parallel surfaces. Separate transmission mea-
 542 surements were taken with bare quartz tiles that were irradiated alongside
 543 the glue samples and showed negligible optical degradation. The transmis-
 544 sion curves for both NOA-61 and RTV-3145 are shown in Figure 5.14. The
 545 comparison of their performance at a wavelength of 420 nm (the peak of the
 546 LYSO:Ce emission spectrum) is shown in 5.14c. NOA-61 provides better
 547 performance prior to irradiation but degrades as the ionizing dose increases.
 548 RTV-3145 is less affected and despite starting with a lower transmission
 549 ends up with a higher transmission after the full ionizing dose. With the
 550 expected thickness of the glue layers in the BTL to be $50 \mu\text{m}$ or thinner,
 551 both glues would have less than 3% loss in transparency and therefore meet
 552 the radiation tolerance requirement.

553 As previously mentioned, the glues would need to withstand temperature
 554 ranges from -40 to +60°C. This was checked by gluing pairs of SiPMs to a
 555 crystal bar and thermally cycled several times between the aforementioned
 556 temperatures. Neither glue showed visible transparency loss nor did they
 557 show any signs of structural degradation such as cracks. The bond created
 558 by both glues remained mechanically strong. The SiPMs glued with NOA-
 559 61 could not be removed from the crystal bar without severely damaging the
 560 SiPMs. Those glued with RTV-3145 could be removed but only by applying
 561 a large amount of torsion. As it is, both glues remain potential candidates as



(a) Teflon mold used to produce glue samples



(b) Glue samples used for preliminary radiation tolerance studies

Fig. 5.11: Left: This is a teflon mold used to produce glue samples. Right: The glue samples after being removed from the mold. These samples were then placed in the irradiator for radiation exposure.

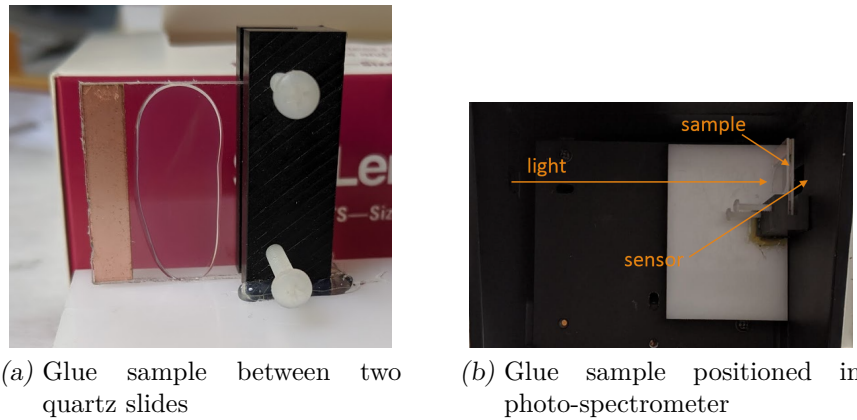
562 they have both surpassed the standards required for usage in the BTL. RTV-
 563 3145 is slightly favored as it was used in the CMS ECAL with good results
 564 and has been shown to be more radiation tolerant than NOA-61. Another
 565 benefit of RTV-3145 over NOA-61 is that the crystal bars will be covered
 566 in a wrapping prior to gluing. This is problematic for NOA-61 because it
 567 requires exposure to UV light in order to cure and this is made difficult by
 568 the opaque wrapping.

569 5.2.4 Performance at test beam

570 Test beam facilities at both CERN and Fermilab were used to test the BTL
 571 sensor prototypes throughout the research and development process. These
 572 facilities provide well calibrated sources of MIPs in the form of high energy
 573 pions at CERN and protons at Fermilab.



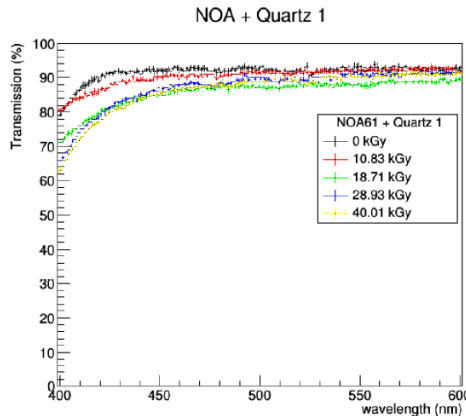
Fig. 5.12: Preliminary radiation tolerance studies of the top five glue candidates show that only NOA-61 and RTV-3145 are viable. Epotek, Polytec, and BC-600 all show substantial optical degradation after just a fraction of 50 kGy target.



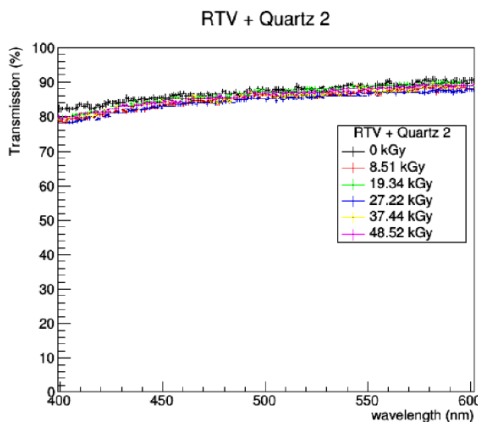
(a) Glue sample between two quartz slides

(b) Glue sample positioned in photo-spectrometer

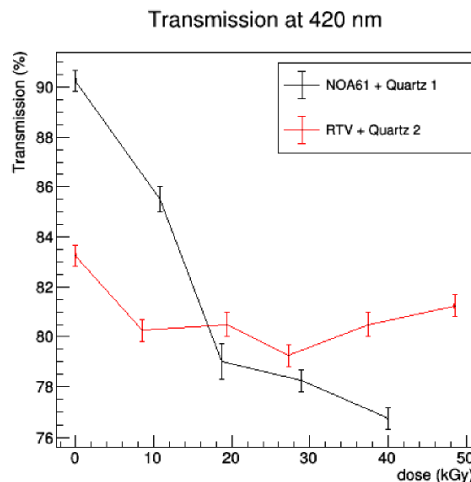
Fig. 5.13: Figure 5.13a shows an example a glue sample ready for transmission measurements. Figure 5.13b shows how the measurement is taken with the sample placed inside the photo-spectrometer.



(a) Optical transmission curves for NOA-61 with increasing doses of radiation



(b) Optical transmission curves for RTV-3145 with increasing doses of radiation



(c) Transmission at wavelength of 420 nm after various ionizing doses

Fig. 5.14: Transmission curves for both NOA-61 (Figure 5.14a and RTV-3145 (Figure 5.14b)). Figure 5.14c shows the transmission at 420 nm, the peak of the LYSO:Ce emission spectrum, with increasing ionizing doses. While NOA-61 starts with a higher transmission, RTV-3145 is more radiation tolerant and has a higher transmission after the full ionizing dose.

574

6. CMS TRIGGER SYSTEM

575 When operating at nominal luminosity the LHC produces over 1 billion
576 proton-proton collisions per second. Finite computing speed and storage
577 capacity limit the rate at which CMS can record events to be about 1 kHz
578 [9]. Decreasing the rate from 1 GHz to 1 kHz is accomplished by using a
579 two-level trigger system to quickly decide which events will be discarded
580 and which will be recorded. The first stage is a hardware-based Level 1 (L1)
581 trigger and the second stage is software-based High Level Trigger (HLT).

582

6.1 *L1 trigger*

583 The L1 trigger decreases the rate by about six orders of magnitude from 1
584 GHz to 100 kHz by performing rough calculations on information from the
585 ECAL, HCAL, and muon subsystems using field-programmable gate arrays
586 (FPGAs). The L1 trigger can be divided further into the calorimeter and
587 muon triggers. The schematic of the L1 trigger system in Figure 6.1 shows
588 both the calorimeter and muon triggers. The calorimeter trigger trigger
589 uses information from the ECAL and HCAL subdetectors to construct pho-
590 ton, electron, and jet candidates in addition to quantities such as missing
591 transverse momentum and total hadronic activity. The muon trigger uses
592 information from all three muon subsystems to construct muon candidates.
593 The outputs from the calorimeter and muon triggers goes into the Global
594 Trigger (GT) which decides which events should be recorded and which are
595 to be discarded [29].

596

6.1.1 *Calorimeter trigger*

597 Trigger Primitives (TP) are the raw inputs from the ECAL and HCAL
598 for the calorimeter trigger. The TP, which contain information regarding
599 the energy deposits in the calorimeters, are passed to the first layer of the
600 calorimeter trigger. This first layer consists of several FPGA cards that
601 receive data from several bunch crossings, but are each mapped to a section
602 of the detector. This data is then passed on to the second layer in such a way

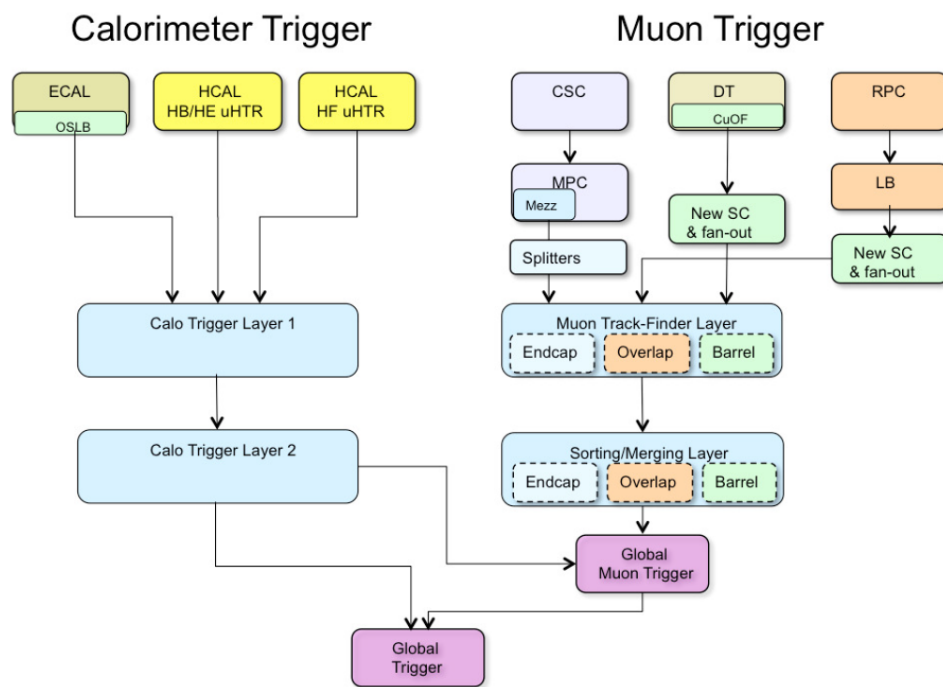


Fig. 6.1: L1 trigger system. Reprint from [3]

603 that each FPGA in this layer will receive data for the entire calorimeter for
604 each bunch crossing. Candidate objects are then constructed and organized
605 into a sorted list according to transverse momentum and passed on to the
606 GT and the global muon trigger.

607 *6.1.2 Muon trigger*

608 TP for the muon trigger come from the three muon detectors, the CSCs,
609 DTs, and RPCs. These are then passed on to the first layer of the muon
610 trigger (Muon Track-Finding Layer) where the TP are combined to recon-
611 struct muon tracks for sections of ϕ for different regions of $|\eta|$. The barrel
612 track-finder for $|\eta| < 0.83$, the endcap track-finder for $|\eta| > 1.24$, and the
613 overlap track-finder for $0.83 < |\eta| < 1.24$. This data is passed on to the
614 second layer where the sections of ϕ are merged and subsequently passed
615 on to the global muon trigger where it is combined with the output from
616 Calo Trigger Layer 2 to compute isolation. The global muon trigger then
617 combines the η regions and passes a list of the top eight muon candidates
618 to the GT.

619 *6.1.3 Global Trigger*

620 Final processing of the reconstructed objects and quantities constructed by
621 the calorimeter and muon triggers is carried out by the GT. L1 algorithms
622 or "seeds" are implemented by the GT using these objects. A full set of L1
623 seed is called a L1 menu and can be adjusted to meet the requirements of
624 the CMS physics program. Each L1 seed can be given a "prescale", which is
625 an integer value N that can be used to reduce the rate of a particular trigger
626 path. This is done by only applying the trigger to one out of N events and
627 can be used to take advantage of the current LHC running conditions.

628 *6.2 High Level Trigger*

629 Events that are accepted by the L1 trigger are passed on to the HLT which
630 is based in software and is therefor capable of analyzing events with a higher
631 degree of sophistication. The HLT has access to information from the full
632 detector and implements "paths" to select events of interest from those pass-
633 ing the L1 trigger. Each HLT path is a set of criteria that is used to either
634 accept or reject an event. The full set of HLT paths is the HLT menu. Each
635 HLT path is "seeded" by one or more L1 seeds in order to decrease comput-
636 ing time. That means that a given HLT path will only be processed if the

637 L1 bits associated with its seed or seeds fire. Each HLT path is assigned to
638 a primary dataset depending on its general physics signature. In the case
639 of this analysis, the primary dataset used for signal events was DoubleEG
640 for years 2016 and 2017. This was merged into the EGamma dataset for
641 2018. The SingleMuon dataset was used for trigger efficiency studies. A list
642 of the primary HLT used for each year along with its associated primary
643 dataset is listed in Table 6.1. The HLT path for 2016 is different because
644 HLT_DoublePhoton70 was not a part of the HLT menu until 2017.

Tab. 6.1: Primary HLT

Year	HLT path	Primary dataset
2016	HLT_DoublePhoton60	DoubleEG
2017	HLT_DoublePhoton70	DoubleEG
2018	HLT_DoublePhoton70	EGamma

645 *6.3 Trigger efficiency*

646 7. CMS PARTICLE AND EVENT RECONSTRUCTION

647 After an event is chosen to be stored by the trigger system, the output from
648 all of the sub-detectors is saved and recorded to disk as "RAW" data. These
649 data contain information about the response of each sub-detector, such as
650 tracker hits and energy deposition in the calorimeters. As was mentioned
651 in Chapter 4, shown in Table 4.1 and Figure 4.2, the CMS was designed
652 such that each type of particle resulting from the pp collisions at the IP
653 would leave a distinct signature in the sub-detectors. This allows for the
654 information to be reconstructed into lists of physics object candidates such
655 as photons, electrons, muons, etc and quantities such as missing transverse
656 momentum. The particle flow (PF) algorithm performs this reconstruction
657 by first building tracks and calorimeter clusters. These two elements are the
658 inputs to the reconstruction of the aforementioned physics object candidates
659 using a "link" algorithm.

660 7.1 *Tracks*

661 A combinatorial track finder algorithm based on the Kalman filtering tech-
662 nique uses the hits in the silicon tracker to reconstruct tracks of charged
663 particles [18]. Each iteration of the algorithm is comprised of three steps:

- 664 • Seed generation: Find a seed consisting of two to three hits that is
665 compatible with a track from a charged particle.
- 666 • Track finding: Use pattern recognition to identify any hits that are
667 compatible with the trajectory implied by the seed generated in the
668 first step.
- 669 • Track fitting: Determine the properties of the track, such as origin,
670 trajectory, and transverse momentum by performing a global χ^2 fit.

671 The first iteration uses stringent requirements on the seeds and the χ^2
672 of the track fit to pick out isolated jets which have very high purity. The
673 hits associated with these high purity tracks are then removed to reduce the

674 combinatorial complexity for subsequent iterations. This allows successive
675 iterations to identify less obvious tracks by progressively loosening criteria
676 while the removal of previously associated hits mitigates the likelihood of
677 fake tracks being built.

678 7.2 Calorimeter clusters

679 Calorimeter clusters are constructed using energy deposition information
680 from the calorimeters. Clusters are formed by first identifying the seed cell
681 (ECAL crystal or HCAL scintillating tile) that corresponds to the local
682 maxima of an energy deposit that is above a given threshold. Neighboring
683 cells are then aggregated to grow topological clusters if their signals are
684 above twice the standard deviation of the level of electronic noise.

685 7.3 Object identification

686 At this point the tracks and calorimeter clusters are linked to form a PF
687 block. This linkage is done with an algorithm that quantifies the likelihood
688 that a given track and cluster were results of the same particle. As PF blocks
689 are identified as object candidates they are removed from the collection prior
690 to each subsequent iteration until all tracks and clusters have been assigned
691 to a PF object candidate. The following sections will outline how each of
692 these PF objects is identified.

693 7.3.1 Muons

694 Muons are the easiest particle to identify, so they are the first objects recon-
695 structed in the CMS. PF Muons are classified in three categories depending
696 on how their tracks are reconstructed:

- 697 • Tracker muons: Tracks reconstructed from the inner tracker having
698 $p_T > 0.5$ GeV and $|\vec{p}| > 2.5$ GeV that, when propagated to the muon
699 system, match at least one hit in the muon chambers.
- 700 • Stand-alone muons: Tracks reconstructed only using hits in the muon
701 system.
- 702 • Global muons: Stand-alone muons that coincide with a track from the
703 inner tracker.

704 After a muon is reconstructed it is given an identification or ID based on
705 observables such as the χ^2 of the track fit, how many hits were recorded

706 per track, or how well the tracker and stand-alone tracks matched. These
707 IDs represent different working points (loose, medium, and tight) which
708 correspond to increasing purity but decreasing efficiency as you move from
709 loose toward tight.

710 **7.3.2 Electrons**

711 The next objects reconstructed in the CMS are electrons. Bremsstrahlung in
712 the tracker layers causes substantial energy loss and changes in momentum
713 which requires the use of a dedicated tracking algorithm. In place of the
714 Kalman filtering technique, a Gaussian-sum filter (GSF) algorithm is used.
715 This algorithm uses a weighted sum of Gaussian PDFs which does a bet-
716 ter job of modeling the Bremsstrahlung effects than the Kalman filtering
717 technique which uses a single Gaussian PDF.

718 PF ECAL clusters are regrouped by identifying a seed cluster then asso-
719 ciating and adding clusters from Bremsstrahlung photons to form superclus-
720 ters. The schematic in Figure 7.1 shows how the Bremsstrahlung photons
721 are emitted in directions tangent to the trajectory of the electron. Electrons
722 bending in the magnetic field causes spreading of PF ECAL clusters to typ-
723 ically occur along the ϕ -direction. Two approaches are used to associate
724 the superclusters to GSF tracks. One is the ECAL-driven method, which
725 uses superclusters with $p_T > 4$ GeV as seeds for the GSF track finding al-
726 gorithm. This works well for high- p_T isolated electrons because the bend
727 radius is less severe which decreases the spread of the PF ECAL clusters.
728 This results in more of the Bremsstrahlung radiation being recovered and
729 correctly associated with an electron candidate. The second approach is the
730 tracker-driven method which uses tracks with $p_T > 2$ GeV as seeds that are
731 propagated out to the surface of the ECAL and used for clustering. This
732 method works best with soft electrons like those in jets because it relies on
733 the high granularity of the tracker to disentangle overlapping energy deposits
734 in the ECAL. [24]

735 As a final step, a boosted decision tree (BDT) is used to discriminate
736 between real and fake electrons. The BDT is given variables associated with
737 track-cluster matching, shower shape, and tracking. The output score of
738 the BDT is used to classify electrons into loose, medium, and tight working
739 points which exhibit the same purity and efficiency trends as the muon
740 working points.

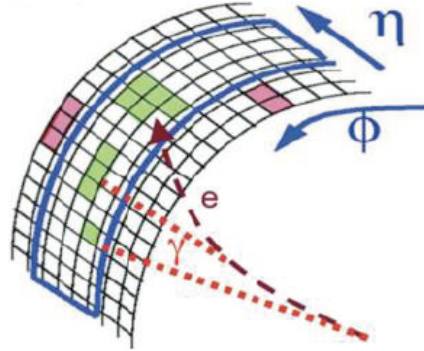


Fig. 7.1: The Bremsstrahlung photons continue along a straight trajectory while the electron path is bent by the magnetic field. This results in energy deposited in the calorimeter for such electrons to be spread out along the ϕ -direction.

741

7.3.3 Photons

742 Unlike electrons, photons typically deposit most of their energy in the ECAL
 743 without interacting with the tracker therefore their reconstruction is seeded
 744 from ECAL superclusters that do not have any GSF tracks associated with
 745 them. When photons interact with the tracker material they convert into
 746 electron-positron pairs which follow bent trajectories due to the magnetic
 747 field prior to entering the ECAL. This causes a spread of the energy deposi-
 748 tion along the ϕ -direction. The goal of the clustering algorithm for photon
 749 reconstruction is to include all of the energy deposits of electrons resulting
 750 from photon conversions. As with the calorimeter clustering algorithm, the
 751 photon clustering starts by identifying a local energy maxima as a seed crys-
 752 tal. In the EB a cluster is made up of several parallel strips of crystals 5×1
 753 in $\eta \times \phi$. The first strip has the seed crystal at its center. Neighboring strips
 754 in the ϕ -direction are added if they have energy above a threshold of 10 GeV
 755 but less than that of the subsequent strip with a maximum of 17 strips in
 756 a cluster. In the EE, the seed cluster is 5×5 with adjacent 5×5 clusters
 757 being added if they meet the minimum energy requirement.

758 Converted and unconverted photons can be differentiated by looking at
 759 how the energy is distributed in a supercluster. The variable R_9 is used for
 760 this purpose. It is defined as the ratio of the energy in a 3×3 crystal array to
 761 the energy in the entire supercluster. As the energy deposits resulting from
 762 converted electrons is more spread out they result in a lower R_9 value than

763 unconverted photons. A photon is candidate is considered to be unconverted
 764 when $R_9 > 0.93$.

765 An important point regarding the clustering algorithm is that it does
 766 not differentiate between showers resulting from photons and those resulting
 767 from electrons. This allows for electron from $Z \rightarrow ee$ events to be used as
 768 high purity samples to study analysis inputs and for defining control regions
 769 using electron in place of photons.

770 7.3.4 Jets

771 When quarks or gluons are produced they hadronize to make cone-shaped,
 772 collimated collections of particles called jets. The jet clustering algorithm
 773 aims to combine these particles in order to accurately measure the kine-
 774 matics of the initial gluon or quark. The algorithm uses the two distance
 775 parameters

$$d_{ij} = \min(k_{T_i}^{2p}, k_{T_j}^{2p}) \frac{\Delta R_{ij}^2}{R^2} \quad (7.1)$$

$$d_{iB} = k_{T_i}^{2p} \quad (7.2)$$

776 where d_{ij} is the distance between objects i and j and d_{iB} is the distance
 777 between object i and the beam B . The transverse momentum of the object is
 778 k_T . The parameter p is set either -1, 0, or +1 to specify whether the anti- k_T ,
 779 inclusive Cambridge/Aachen, or inclusive k_T algorithm is used, respectively.
 780 The value of ΔR_{ij}^2 is defined as $(\eta_i - \eta_j)^2 + (\phi_i - \phi_j)^2$ and R is the distance
 781 parameter that defines the radius of the jet.

782 his analysis uses jets reconstructed from PF candidates using the anti- k_T
 783 algorithm with $R = 0.4$, also known as AK4PFJets or just PFJets. The
 784 algorithm goes through the following steps:

- 785 1. The smallest values of d_{ij} and d_{iB} are computed for all objects in the
 786 event.
- 787 2. Objects i and j are merged into a single object if $d_{ij} < d_{iB}$.
- 788 3. Object i is labeled as a jet and removed from the list if $d_{iB} < d_{ij}$.

789 Note for next time: Now talk about infrared and collinear safe. Use
 790 Allie's thesis for guide. Look at "recent thesis" for ECAL noise on 2017
 791 data. Should also do JEC and JER in here.

792 7.4 Missing transverse momentum

8. DATA ANALYSIS

8.1 Overview

This analysis is motivated by the GGM supersymmetry breaking scenario in which the strong production of either gluinos or squarks result in a final state containing two photons, jets, and missing transverse momentum. Two example topologies are shown in Figure 8.1. If the T5gg model, each of the produced gluinos decays to a neutralino which then decays to a photon and a gravitino. Similarly, the T6gg model has each of the produced squarks decays to a neutralino which then decays to a photon and a gravitino. In both cases the gravitino escapes the CMS without detection which manifests as missing transverse momentum.

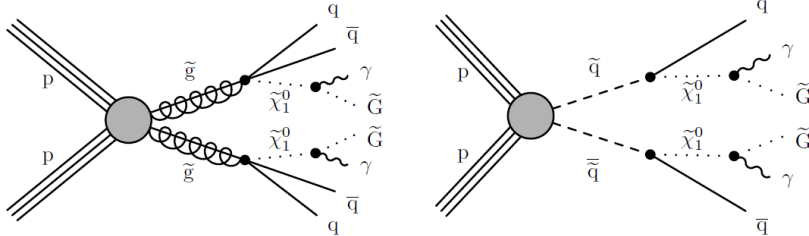


Fig. 8.1: Two examples of GGM supersymmetry breaking processes resulting in final states containing two photons and missing transverse momentum. The T5gg model (left) shows gluinos produced from $p - p$ collisions which subsequently result in two neutralinos, each decaying to a photon and a gravitino. The T6gg model (right) shows squarks produced from $p - p$ collisions following a similar decay chain.

8.2 Data

This analysis was performed using 137 fb^{-1} of data collected from the CMS detector during the time period commonly referred to as Run 2 which spans from 2016 to 2018. The complete list of the datasets used can be found in

808 Table 8.1. The JSON files used to identify events passing all of the CMS
 809 offline data quality monitoring requirements are:

810 Cert_271036_284044_13TeV_23Sep2016ReReco_Collisions16_JSON.txt
 811 Cert_294927_306462_13TeV_EOY2017ReReco_Collisions17_JSON_v1.txt
 812 Cert_314472_325175_13TeV_PromptReco_Collisions18_JSON.txt

Tab. 8.1: Data Samples

/DoubleEG/Run2016B-17July2018-ver2-v1
/DoubleEG/Run2016C-17July2018-v1
/DoubleEG/Run2016D-17July2018-v1
/DoubleEG/Run2016E-17July2018-v1
/DoubleEG/Run2016F-17July2018-v1
/DoubleEG/Run2016G-17July2018-v1
/DoubleEG/Run2016H-17July2018-v1
/DoubleEG/Run2017B-31Mar2018-v1
/DoubleEG/Run2017C-31Mar2018-v1
/DoubleEG/Run2017D-31Mar2018-v1
/DoubleEG/Run2017E-31Mar2018-v1
/DoubleEG/Run2017F-31Mar2018-v1
/EGamma/Run2018A-17Sep2018-v2
/EGamma/Run2018B-17Sep2018-v1
/EGamma/Run2018C-17Sep2018-v1
/EGamma/Run2018D-22Jan2019-v2

813

8.3 Monte Carlo samples

814 Monte Carlo (MC) simulation were used to validate performance of the
 815 analysis on backgrounds, model background contributions, constructing a
 816 multivariate discriminant, and determining signal efficiencies.

817

8.4 Object definitions

818 The object candidates that are identified by the reconstruction algorithms
 819 are subject to further scrutiny in order to achieve optimal purities in the
 820 offline analysis.

821 8.4.1 Photons

822 Photons are required to have $p_T > 75$ GeV and meet the criteria prescribed
 823 by loose ID cuts derived by the e/γ Physics Object Group (EGM POG).
 824 The cut variables used to determine the photon ID are:

- 825 • H/E - The ratio of the energy deposited in the HCAL tower that is
 826 directly behind the ECAL supercluster associated with the photon to
 827 the energy deposited in the ECAL supercluster.
- 828 • $\sigma_{i\eta i\eta}$ - The log-fractional weighted width of a shower in $i\eta$ -space. This
 829 variable is used to describe the shower shape.
- 830 • Particle Flow Charged Isolation - Sum of the p_T of charged hadrons
 831 associated with the primary vertex within a cone of $0.02 < \Delta R < 0.3$
 832 of the supercluster.
- 833 • Particle Flow Neutral Isolation - Sum of the p_T of neutral hadrons
 834 associated with the primary vertex within a cone of $\Delta R < 0.3$ of the
 835 supercluster.
- 836 • Particle Flow Photon Isolation - Sum of the p_T of photons within a
 837 cone of $\Delta R < 0.3$ of the supercluster.

838 All of the isolation variables listed above are corrected in order to remove
 839 pileup. Table 8.2 gives a summary of the pileup-corrected requirements for a
 840 loose ID photon. The loose ID working point has an efficiency (background
 841 rejection) of 90.08% (86.25%) in the barrel and 90.65% (76.72%) in the end
 842 caps. In addition to the p_T and loose ID requirements, a photon must also
 843 pass a pixel seed veto (PSV). This means that there is no pixel seed matched
 844 to the photon.

Tab. 8.2: Summary of loose ID photons cuts

Variable	Cut Value (Barrel)	Cut Value (Endcap)
H/E	0.04596	0.0590
$\sigma_{i\eta i\eta}$	0.0106	0.0272
Charged Iso	1.694	2.089
Neutral Iso	$24.032 + 0.01512 p_{T\gamma} + 2.259 \times 10^{-5} p_{T\gamma}^2$	$19.722 + 0.0117 p_{T\gamma} + 2.3 \times 10^{-5} p_{T\gamma}^2$
Photon Iso	$2.876 + 0.004017 p_{T\gamma}$	$4.162 + 0.0037 p_{T\gamma}$

845

8.4.2 Electrons

846 As mentioned earlier, the clustering algorithm doesn't differentiate between
847 showers from photons and those from electrons. In this analysis an electron
848 is defined as an object that passes all of the photon requirements except
849 for the PSV. Inverting the pixel seed requirement while using the same ID
850 criteria ensures that we have orthogonal selections while minimizing the
851 bias potentially introduced by using control regions with electrons to model
852 diphoton signal regions.

853

8.4.3 Muons

854

8.4.4 Jets

855 Jets are reconstructed using the anti- k_T algorithm described in Chapter 7
856 within a cone having radius $R = 0.4$. The nature of this reconstruction also
857 labels the previously mentioned objects (photons, electrons, and muons) as
858 jets so these need to be removed from the jet collection. This process is
859 called "cleaning" the jets.

860

8.5 Backgrounds

861 The sources of background in this analysis can be grouped into three cate-
862 gories. In order of decreasing contribution they are mismeasured hadronic
863 activity, electrons misidentified as photons, and standard model processes
864 having final states with neutrinos and two photons. In events with mul-
865 tiple jets, limitations on the jet energy resolution can give rise to an ap-
866 parent imbalance in p_T as is shown in Figure 8.2. Such events are usually
867 from quantum chromodynamics (QCD) processes. In these cases jets can
868 be misidentified as photons or there can be real photons being produced.
869 In both cases the result is the appearance of two photons accompanied by
870 E_T^{miss} which mimics our signal. Given the large cross-section for QCD, this
871 is the most significant background in this analysis. The next background,
872 resulting from the misidentification of electrons as photons, comes from elec-
873 troweak (EWK) processes, in particular $W\gamma$ and $W + \text{jets}$ events where
874 $W \rightarrow e\nu$. Here the neutrino contributes real E_T^{miss} while the fake photon
875 allows this event to fulfill the diphoton requirement. The final background
876 is from $Z\gamma\gamma \rightarrow \nu\nu\gamma\gamma$ events, which exactly mimic our signal, and is modeled
877 using simulation as it is irreducible.

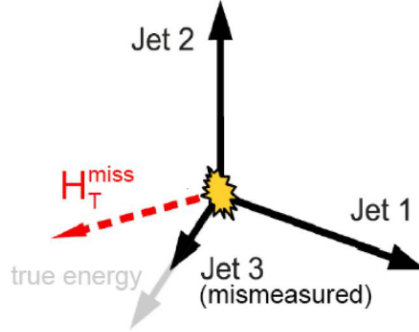


Fig. 8.2: Mismeasurement of Jet3 results in an imbalance in the events transverse momentum.

878

8.5.1 Instrumental background

879 The instrumental background is the contribution from events with spurious
 880 E_T^{miss} due to mismeasured hadronic activity. The vast majority of interac-
 881 tions produced from proton-proton collisions at the LHC are hadronically
 882 rich QCD events. Aside from some very rare final states with heavy-flavor
 883 jets, these events do not include neutrinos, which are the only stable particles
 884 in the SM that pass through the CMS detector unobserved, and therefore
 885 exhibit little or no E_T^{miss} at the parton level. However, the measurements of
 886 final-state particles are made using the tracker and calorimeters which have
 887 finite energy and momentum resolution. These limitations propagate into
 888 the calculation of E_T^{miss} leading to an inequality between the real, parton
 889 level E_T^{miss} in an event and the measured E_T^{miss} . Since most of this back-
 890 ground is comprised of QCD events, it is commonly referred to as the "QCD
 891 background" and those terms are used interchangeably in this thesis. Mod-
 892 eling of this background was done using the Rebalance and Smear technique
 893 while a multivariate discriminant was constructed to improve the efficiency
 894 of identifying events with fake E_T^{miss} .

895

Rebalance and smear

896 The rebalance and smear method is used to model the spurious E_T^{miss} back-
 897 ground. The general idea is to rebalance the collection of measured jets
 898 such that it reproduces what is seen at the parton level and then smear the
 899 rebalanced jets in a way consistent with the known jet energy resolutions to
 900 return the rebalanced event to a more detector-like event.

901 Coming soon....

902 *Multivariate discriminant*

903 A boosted decision tree (BDT) was used to develop a discriminating variable
 904 for identifying events with real E_T^{miss} . Training and testing of the BDT was
 905 performed in ROOT using the Toolkit for MultiVariate Analysis (TMVA).
 906 The signal samples used for both training and testing are comprised of a
 907 combination of different mass points from the T5Wg and T6Wg MC sam-
 908 ples. The mass points used were chosen to represent a wide range of mass
 909 differences between gluino/squark and neutralino masses. This was done by
 910 using the bands of gluino/squark masses shown in Figure 8.3. In order to
 911 minimize any bias in the BDT response to model-dependent parameters like
 912 the difference between gluino/squark and neutralino masses, the training
 913 events used from each mass point were weighted by a factor one over the
 914 number events generated for that particular model. This ensures that each
 915 mass point in the mass band is equally represented in the training sample
 916 for the BDT. The location of the mass bands were chosen to be near the
 917 edge of the exclusion region to target the phase space not yet ruled out by
 918 previous analyses. The background samples use for training and testing of
 919 the BDT were GJets MC samples that had been Rebalanced and Smeared
 920 to increase statistics. These simulate Standard Model processes resulting in
 921 final states containing jets and at least one photon which is the source of the
 922 fake E_T^{miss} background. The full list of MC samples used in the BDT train-
 923 ing can be seen in Table 8.3. For events from these samples to be included
 924 in the training or testing of the BDT, they were required to have

- 925 • At least two photons without associated pixel seeds as described in
 926 Section 8.4.1.
- 927 • At least one of those photons is in the EB ($|\eta| < 1.44$)
- 928 • Both photons within the range of tracker acceptance ($|\eta| < 2.4$)
- 929 • At least two jets as described in Section 8.4.4.
- 930 • Hard $E_T^{miss} > 130$ GeV

931 The input variables used by the BDT are listed below. All energy and
 932 momentum variables were normalized to the scalar sum of all of the p_T in
 933 the event $S_T = \sum_{\gamma, jets} |\vec{p}_T|$ in order to encourage the BDT to focus more
 934 on how the energy and momentum was distributed in an event rather than
 935 simply the scale of the energy or momentum.

Tab. 8.3: List of MC samples used for training and testing BDT

Signal Samples
SMS-T5Wg_TuneCUETP8M1_13TeV-madgraphMLM-pythia8
SMS-T6Wg_TuneCUETP8M1_13TeV-madgraphMLM-pythia8
Background Sample
GJets_DR-0p4_HT-100To200_TuneCUETP8M1_13TeV-madgraphMLM-pythia8
GJets_DR-0p4_HT-200To400_TuneCUETP8M1_13TeV-madgraphMLM-pythia8
GJets_DR-0p4_HT-400To600_TuneCUETP8M1_13TeV-madgraphMLM-pythia8
GJets_DR-0p4_HT-600ToInf_TuneCUETP8M1_13TeV-madgraphMLM-pythia8

- 936 • $S_{T_{jets}} = \sum_{jets} |\vec{p}_T|$
- 937 • $p_{T_{jets}} = \sum_{jets} \vec{p}_T$
- 938 • $p_{T_{\gamma\gamma}} = \vec{p}_{T_{\gamma_1}} + \vec{p}_{T_{\gamma_2}}$
- 939 • $HardE_T^{miss} = - \sum_i \vec{p}_T_i$
- 940 • $\Delta\Phi_{\gamma\gamma} = \Delta\Phi(\vec{p}_{T_{\gamma_1}}, \vec{p}_{T_{\gamma_2}})$
- 941 • $\Delta\Phi_{min} = min[\Delta\Phi(\vec{p}_{T_{HardE_T^{miss}}}, \vec{p}_{T_{jet_i}})]$
- 942 • $\Delta\Phi_1 = \Delta\Phi(\vec{p}_{T_{HardE_T^{miss}}}, \vec{p}_{T_{jet_1}})$
- 943 • $\Delta\Phi_2 = \Delta\Phi(\vec{p}_{T_{HardE_T^{miss}}}, \vec{p}_{T_{jet_2}})$
- 944 • $\Delta\Phi_{\gamma\gamma, HardE_T^{miss}} = \Delta\Phi(\vec{p}_{T_{HardE_T^{miss}}}, \vec{p}_{T_{\gamma\gamma}})$
- 945 • Add the delta R stuff...

946 Events in both the signal and background samples are randomly split
 947 into either a test or training categories. A substantial difference between the
 948 test and training distributions of the BDT response implies that the BDT
 949 is not drawing reliable conclusions as to whether an event is signal-like or
 950 background-like. A grid search over different combinations of hyperparamete-
 951 rs (the maximum depth of a tree and the number of trees) was performed
 952 to maximize separation between the signal and background BDT response
 953 distributions while maintaining good agreement between the training and
 954 test samples. Using 200 trees with a maximum depth of 4 was found to be
 955 the optimal choice as increasing either or both of those parameters resulted
 956 in over-training with minimal gains in separation of signal and background.

957 The comparison of BDT scores between signal and background events is
 958 shown in Figure 8.5. The training and test samples show good agreement
 959 while there is good separation between signal and background.

960 Using the BDT we created one control region (low BDT score) and two
 961 signal regions (medium and high BDT scores) by defining two BDT score
 962 thresholds. The low threshold corresponds to the minimum BDT score with
 963 at least 90% acceptance of every signal model or mass point in signal MC
 964 samples. Figures 8.6 and 8.7 show the BDT cuts that resulted in 90%
 965 acceptance at each mass point for the T5GG and T6GG models respectively.
 966 In both models the value of this BDT cut is always greater than -0.13 so
 967 this was chosen as the value separating the low-BDT control region and
 968 the medium-BDT signal region. The threshold for the high-BDT region is
 969 chosen such that 90% of the fake E_T^{miss} background from the GJets MC is
 970 excluded. The BDT response for Rebalanced and Smeared events in this
 971 sample is shown in Figure 8.8 where 90% of the events have a score less
 972 than 0.03. This puts the threshold for the high-BDT signal region at a BDT
 973 score of 0.03. With these three regions we have a very background-pure
 974 control region ($\text{BDT} \leq -0.13$) and two signal regions, one very pure in
 975 signal ($\text{BDT} > 0.03$) and one intermediate ($-0.13 < \text{BDT} \leq 0.03$), which
 976 combined have at least 90% acceptance for all mass points.

977 8.5.2 Electroweak background

978 The electroweak background is dominated by events with $W \rightarrow e\nu$ where
 979 the electron is misidentified as a photon. Unlike the QCD background these
 980 events have real E_T^{miss} due to the presence of a neutrino. The key to estimat-
 981 ing this background is determining the rate at which electrons get incorrectly
 982 labeled as photons in the signal region. This is done using a tag-and-probe
 983 method where the tag is an electron (a loose ID photon that fails the PSV)
 984 and the probe is categorized as either a photon or an electron. The result
 985 is an electron-electron region (ee) and an electron-photon region ($e\gamma$) that
 986 are selected from the data. As both of these regions contain $Z \rightarrow ee$ decays,
 987 fits are applied in each of the samples to the invariant mass spectra m_{ee} and
 988 $m_{e\gamma}$. The integrals of these fits are calculated over the range of the Z mass
 989 peak to give the number of events in each category.

990 8.5.3 Irreducible background

991 The irreducible $Z\gamma\gamma \rightarrow \nu\nu\gamma\gamma$ background produces two photons and has
 992 inherent E_T^{miss} via the neutrinos. There is no easy way to separate these

events from our signal so it is estimated using MC simulation. The modeling of this background was tested using $Z\gamma\gamma \rightarrow \mu\mu\gamma\gamma$ and $Z\gamma\gamma \rightarrow ee\gamma\gamma$ events in data. Di-muon events with $|m_{\mu\mu} - m_Z| < 15$ GeV and di-electron events with $|m_{ee} - m_Z| < 15$ GeV were selected and the contribution of the muons/electrons was removed from the E_T^{miss} calculation to mimic $Z \rightarrow \nu\nu$. The event selection criteria for this $Z\gamma\gamma \rightarrow LL\gamma\gamma$ control region was

- 2 looseID photons with $p_T > 30$ GeV
- 2 like-flavored leptons with $p_T > 30$ GeV
- 1001 2 mediumID muons or
- 1002 2 electrons (looseID photons with a pixel seed).

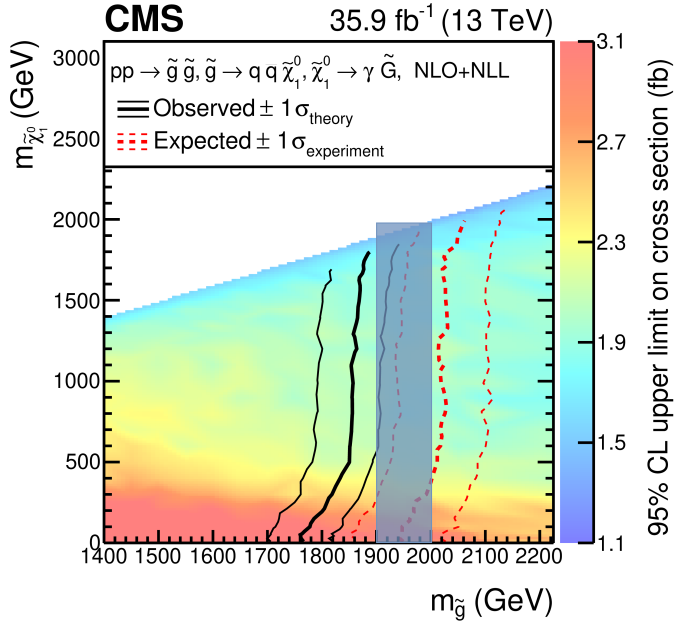
The relationship

$$N_{Z \rightarrow \nu\nu} = \frac{b_{Z \rightarrow \nu\nu}}{b_{Z \rightarrow ee} + b_{Z \rightarrow \mu\mu}} (N_{Z \rightarrow ee} + N_{Z \rightarrow \mu\mu}) \quad (8.1)$$

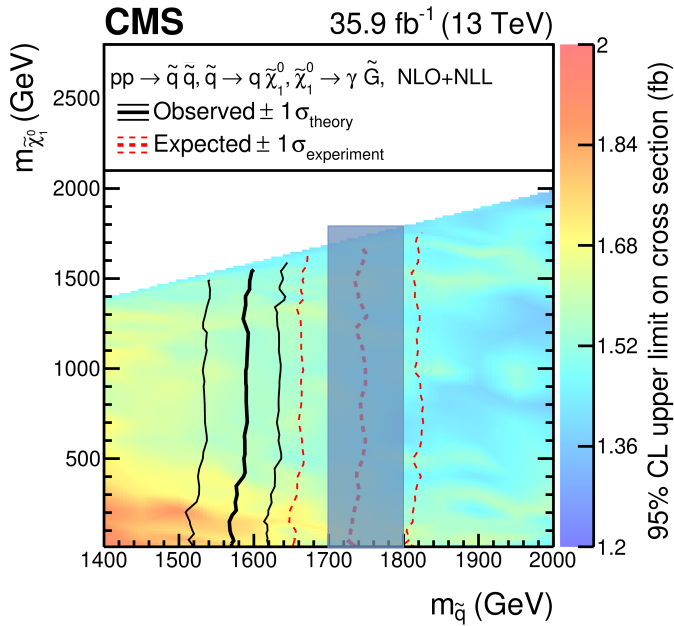
gives an estimation for the number of $Z\gamma\gamma \rightarrow \nu\nu\gamma\gamma$ events expected given the number of $Z\gamma\gamma \rightarrow LL\gamma\gamma$ events observed in data where $N_{Z \rightarrow ee}$ and $N_{Z \rightarrow \mu\mu}$ are the number of data events passing the aforementioned selection criteria and $b_{Z \rightarrow \nu\nu}$, $b_{Z \rightarrow \mu\mu}$, and $b_{Z \rightarrow ee}$ are the branching ratios. The results are summarized in Table 8.4.

Tab. 8.4: Summary of $Z\gamma\gamma \rightarrow \nu\nu\gamma\gamma$ model validation

Year	Data-driven estimation	MC estimation	$\frac{\text{data-driven}}{\text{MC}}$
2016	$30.2 +12.1 -9.0$	33.8 ± 0.31	$0.893 +0.358 -0.267$
2017	-	-	-
2018	-	-	-



(a) Cross-section upper limits for gluino pair production



(b) Cross-section upper limits for squark pair production

Fig. 8.3: The 95% confidence level upper limits on the pair production cross sections for gluinos (8.3a) and squarks (8.3b) as a function of gluino/squark and neutralino masses as reported in [26]. The shaded vertical bands show the mass bands used in the BDT training.

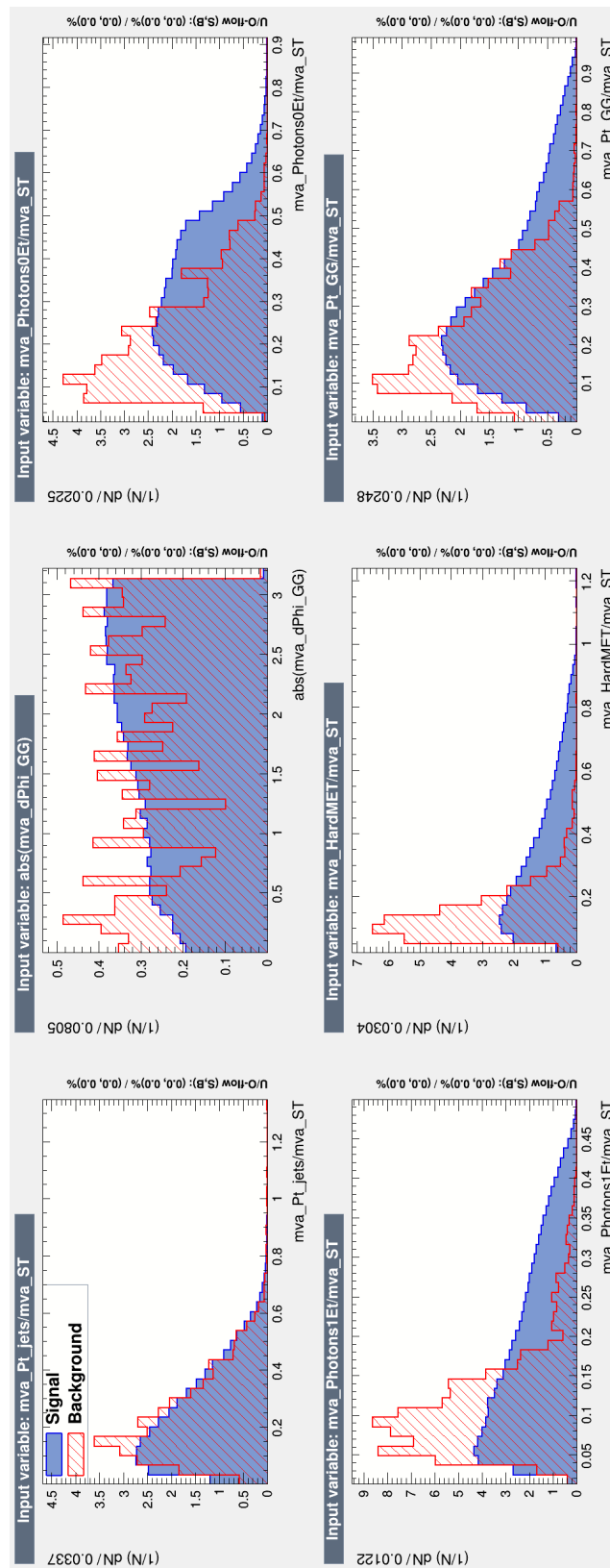


Fig. 8.4: Input variables for the BDT

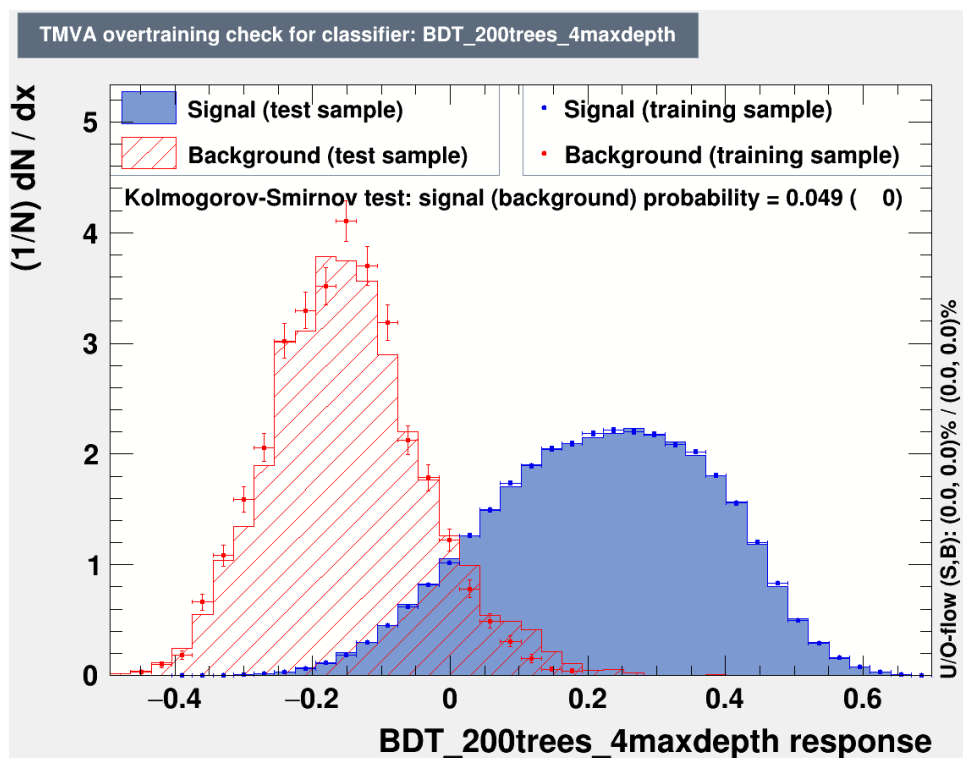


Fig. 8.5: BDT score distributions for signal (blue) and background (red) events. The shaded area shows the distribution of events in the test samples while the dots represent events in the training samples.

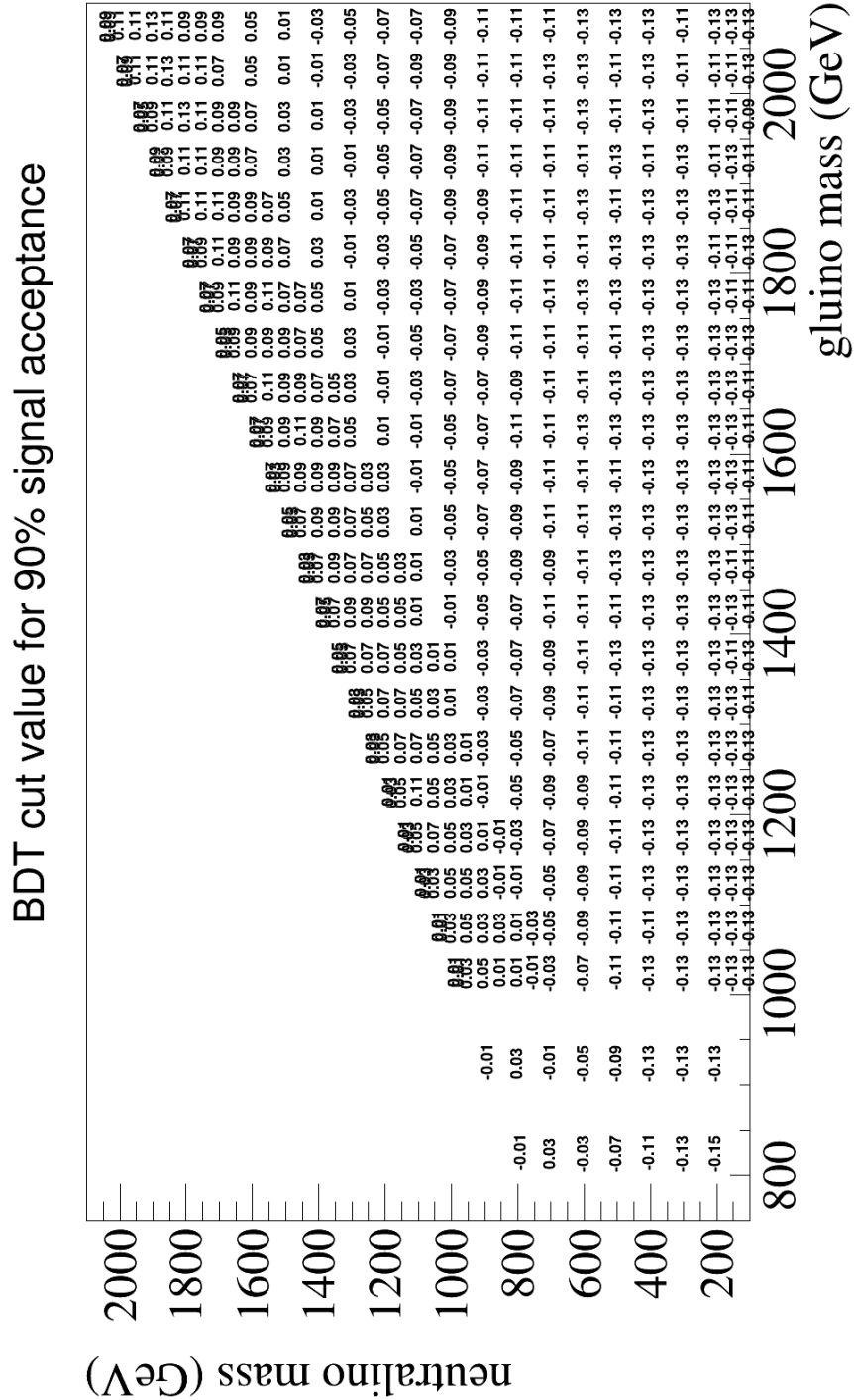


Fig. 8.6: BDT cut values on T5GG models resulting in 90% signal acceptance.

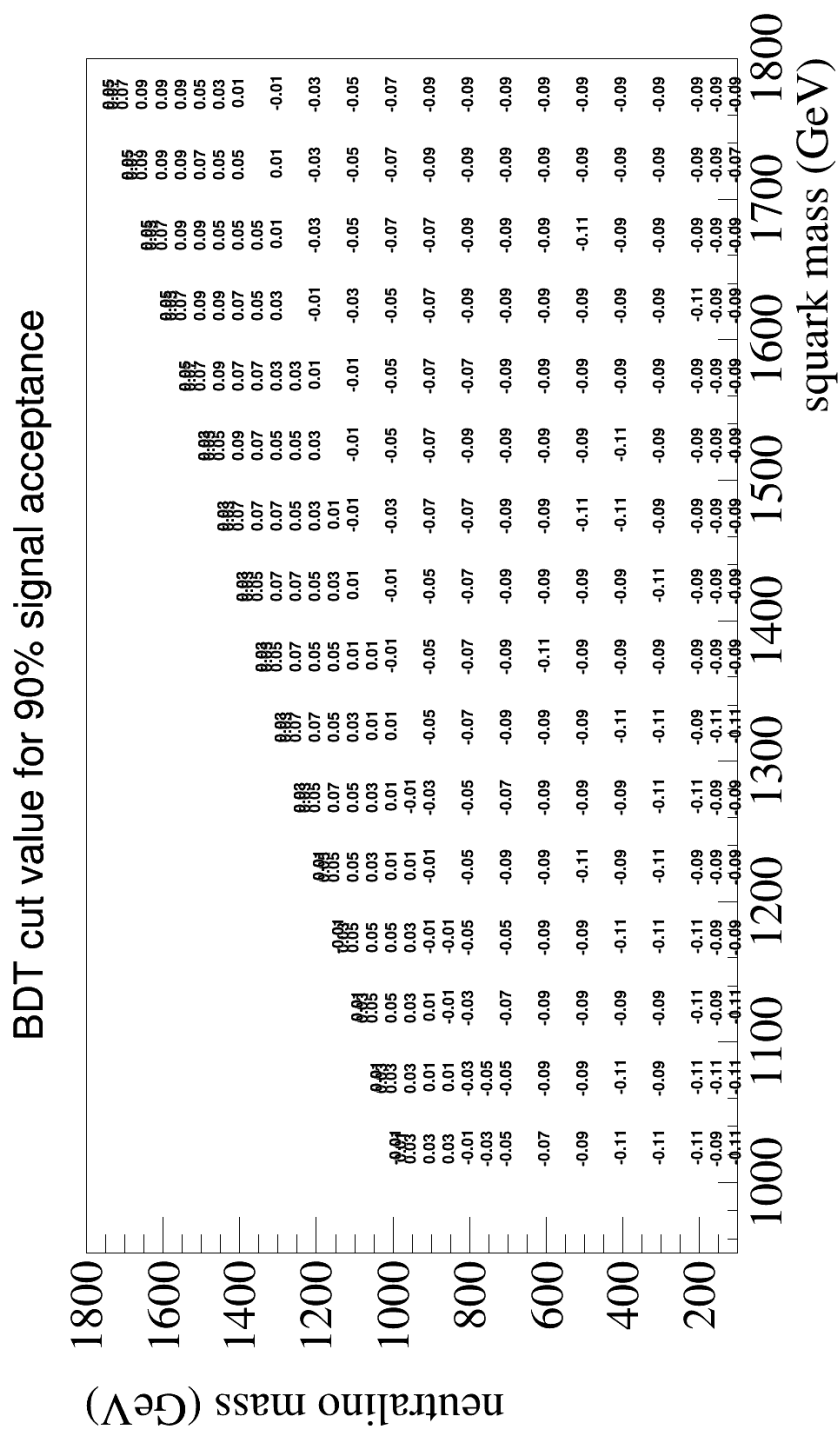


Fig. 8.7: BDT cut values on T6GG models resulting in 90% signal acceptance.

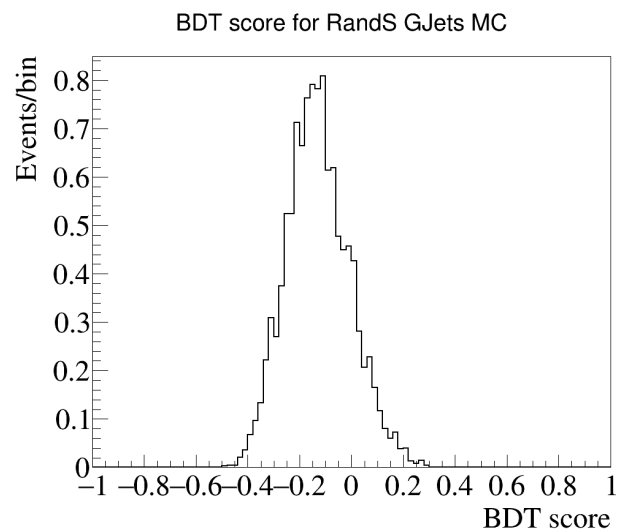


Fig. 8.8: This is the BDT score distribution for Rebalance and Smear events from the GJets MC samples. Requiring a BDT score above 0.03 removes 90% of this background.

BIBLIOGRAPHY

- [1] *The CMS electromagnetic calorimeter project: Technical Design Report.* Technical design report. CMS. CERN, Geneva, 1997.
- [2] *The CMS hadron calorimeter project: Technical Design Report.* Technical design report. CMS. CERN, Geneva, 1997.
- [3] CMS Technical Design Report for the Level-1 Trigger Upgrade. 6 2013.
- [4] S. Abdullin et al. The CMS barrel calorimeter response to particle beams from 2-GeV/c to 350-GeV/c. *Eur. Phys. J. C*, 60:359–373, 2009. [Erratum: Eur.Phys.J.C 61, 353–356 (2009)].
- [5] L. Alvarez-Gaume and J. Ellis. Eyes on a prize particle. *Nature Phys*, 7:2–3, 2011.
- [6] G. Apollinari, O. Brüning, T. Nakamoto, and Lucio Rossi. High Luminosity Large Hadron Collider HL-LHC. *CERN Yellow Rep.*, (5):1–19, 2015.
- [7] S Baird. Accelerators for pedestrians; rev. version. Technical Report AB-Note-2007-014. CERN-AB-Note-2007-014. PS-OP-Note-95-17-Rev-2. CERN-PS-OP-Note-95-17-Rev-2, CERN, Geneva, Feb 2007.
- [8] David Barney. CMS Slice. Feb 2015.
- [9] L. Cadamuro. The CMS Level-1 trigger system for LHC Run II. *JINST*, 12(03):C03021, 2017.
- [10] Jean-Luc Caron. Cross section of lhc dipole.. dipole lhc: coupe transversale. ”AC Collection. Legacy of AC. Pictures from 1992 to 2002.”, May 1998.
- [11] S Chatrchyan et al. Precise Mapping of the Magnetic Field in the CMS Barrel Yoke using Cosmic Rays. *JINST*, 5:T03021, 2010.

- [12] CMS Collaboration. CMS Technical Design Report for the Pixel Detector Upgrade. Technical Report CERN-LHCC-2012-016. CMS-TDR-11, Sep 2012. Additional contacts: Jeffrey Spalding, Fermilab, Jeffrey.Spalding@cern.ch Didier Contardo, Universite Claude Bernard-Lyon I, didier.claude.contardo@cern.ch.
- [13] CMS Collaboration. Description and performance of track and primary-vertex reconstruction with the CMS tracker. *JINST*, 9(CMS-TRK-11-001. CERN-PH-EP-2014-070. CMS-TRK-11-001):P10009. 80 p, May 2014. Comments: Replaced with published version. Added journal reference and DOI.
- [14] The CMS Collaboration. The CMS experiment at the CERN LHC. *Journal of Instrumentation*, 3(08):S08004–S08004, aug 2008.
- [15] The CMS collaboration. The performance of the CMS muon detector in proton-proton collisions at $\sqrt{s}=7$ TeV at the LHC. *Journal of Instrumentation*, 8(11):P11002–P11002, nov 2013.
- [16] Cinzia De Melis. Timeline for the LHC and High-Luminosity LHC. Frise chronologique du LHC et du LHC haute luminosité. Oct 2015. General Photo.
- [17] Lyndon Evans and Philip Bryant. LHC machine. *Journal of Instrumentation*, 3(08):S08001–S08001, aug 2008.
- [18] R. Fruhwirth. Application of Kalman filtering to track and vertex fitting. *Nucl. Instrum. Meth. A*, 262:444–450, 1987.
- [19] Murray Gell-Mann. A Schematic Model of Baryons and Mesons. *Phys. Lett.*, 8:214–215, 1964.
- [20] J. Goldstone. Field Theories with Superconductor Solutions. *Nuovo Cim.*, 19:154–164, 1961.
- [21] S. Gundacker, R. M. Turtos, E. Auffray, and P. Lecoq. Precise rise and decay time measurements of inorganic scintillators by means of X-ray and 511 keV excitation. *Nucl. Instrum. Meth. A*, 891:42–52, 2018.
- [22] Peter W. Higgs. Broken Symmetries and the Masses of Gauge Bosons. *Phys. Rev. Lett.*, 13:508–509, 1964.
- [23] Yutaro Iiyama. *Search for Supersymmetry in pp Collisions at $\sqrt{s} = 8$ TeV with a Photon, Lepton, and Missing Transverse Energy*. PhD thesis, Carnegie Mellon U., 2 2015.

- [24] Jonas Rembser. CMS Electron and Photon Performance at 13 TeV. *J. Phys.: Conf. Ser.*, 1162(1):012008. 8 p, 2019.
- [25] Tai Sakuma and Thomas McCauley. Detector and event visualization with SketchUp at the CMS experiment. *Journal of Physics: Conference Series*, 513(2):022032, jun 2014.
- [26] Albert M Sirunyan et al. Search for supersymmetry in final states with photons and missing transverse momentum in proton-proton collisions at 13 TeV. *JHEP*, 06:143, 2019.
- [27] A.M. Sirunyan et al. Performance of the CMS muon detector and muon reconstruction with proton-proton collisions at $\sqrt{s}=13$ TeV. *Journal of Instrumentation*, 13(06):P06015–P06015, jun 2018.
- [28] Steven Weinberg. The Making of the standard model. *Eur. Phys. J. C*, 34:5–13, 2004.
- [29] J. Wittmann, B. Arnold, H. Bergauer, M. Jeitler, T. Matsushita, D. Rabady, B. Rahbaran, and C.-E. Wulz. The upgrade of the CMS global trigger. *Journal of Instrumentation*, 11(02):C02029–C02029, feb 2016.
- [30] Chen-Ning Yang and Robert L. Mills. Conservation of Isotopic Spin and Isotopic Gauge Invariance. *Phys. Rev.*, 96:191–195, 1954.
- [31] G. Zweig. *An SU(3) model for strong interaction symmetry and its breaking. Version 2.* 2 1964.